communications materials

A Nature Portfolio journal

Review article

https://doi.org/10.1038/s43246-025-00907-y

Progress towards efficient MXene sensors

Check for updates

Ya Yao[1,5], Xinnian Li[2,5], Kim Marie Sisican[2], Rufus Mart Ceasar Ramos[2], Mia Judicpa[2], Si Qin[2], Jizhen Zhang[2,3], Juming Yao[1] ✉, Joselito M. Razal[2,4] ✉ & Ken Aldren S. Usman[2] ✉

MXenes, a new class of two-dimensional transition metal carbides and nitrides, have gained significant research attention due to their exceptional physicochemical properties, making them attractive as active materials for sensing applications. These sensors have diverse uses, including gas sensors for pollutants, biosensors for diagnostics, strain sensors for wearables, and optical sensors for light or chemical changes. They leverage on MXene's unique conductivity, surface and redox reactivity, optoelectronic properties, and thermal behaviour, highlighting their versatility across various technologies. Despite progress, key challenges such as material limitations, processing difficulties, limited real-world testing, and lack of scalable manufacturing, still hinder commercial adoption. This review summarizes the recent progress in MXene-based sensors, examines these challenges, and aims toward the development of cost-effective, high-performance sensors for soft electronics. It also provides guidance for the future development of more efficient sensors and aims to inspire innovations in the field.

MXenes, a family of two-dimensional (2D) transition metal carbides and/or nitrides, have gained considerable attention across various fields due to their highly processable layered structure and remarkable physicochemical properties[1–3]. Since 2011, over 50 MXene compositions have been reported, with many unique carbide/carbonitride combinations theoretically predicted ($M_{n+1}X_nT_x$, where $n = 1–4$, M = transition metal, X = carbon and/or nitrogen, and T = surface functional groups such as –O–, =O, –OH, –F, –Cl)[4,5]. One widely studied example is $Ti_3C_2T_x$ MXene, which stands out among 2D nanomaterials for its exceptional electrical conductivity (>20,000 cm^{-1})[6–8], electrochemical behavior (e.g. capacitance > 2800 F cm^{-3})[9–11], surface reactivity, opto-electronic properties, and thermal stability. This combination of properties makes MXenes highly suitable for diverse sensing applications, including gas sensors for detecting pollutants[12] and toxic gases[13], biosensors for medical diagnostics[14] and health monitoring[15], strain sensors for wearable electronics[16], and optical sensors for detecting light or chemical changes[17]. Recent studies have focused on enhancing the selectivity and sensitivity of MXenes through surface functionalization[18], structural modifications[19] (e.g., doping), and composite formation[20,21].

Incorporating MXene into a host material does not diminish its exceptional properties, unlike most other 2D nanomaterials[22,23], enabling molecular imprinting of polymers[24] or decoration of ligands[25] on the sheet surface without losing conductivity. These surface modifications can create additional active sites for analyte interaction, thereby improving detection capability, selectivity, and overall sensing performance. Likewise, incorporating MXene into polymer matrices improves their electrical conductivity, even with low MXene loading, resulting in durable, lightweight, and highly sensitive physical sensors ideal for wearable electronics[26–28], healthcare monitoring[29], and soft robotics applications[30,31].

Advancements in improving the performance of MXene-based sensors have laid the groundwork for their potential commercialization[21,32,33]. However, achieving industrial-scale production necessitates overcoming key challenges, such as MXenes' susceptibility to oxidative degradation. Achieving multifunctionality requires balancing properties without compromising performance. Scalability remains a challenge due to the complex synthesis and fabrication processes, which must be understood and optimized for large-scale manufacturing while maintaining material properties. This review offers insights into these relevant obstacles to identify methods that enhance sensor performance while uncovering the fundamental and practical limitations of existing MXene-based sensing materials. It also critically analyzes how these factors impact the fabrication of target sensing platforms, aiming to resolve performance issues related to material defects and architectural mismatch. Addressing these impediments is expected to accelerate the development of next-generation MXene-based sensors.

[1]School of Materials Science and Engineering, Zhejiang Sci-Tech University, Hangzhou, China. [2]Institute for Frontier Materials, Deakin University, Waurn Ponds, Burwood, VIC, Australia. [3]Research Center for Materials Nanoarchitectonics, National Institute for Materials Science, Tsukuba, Japan. [4]Joint Research Centre for Fiber Innovations and Renewable Materials, School of Fashion and Textiles, The Hong Kong Polytechnic University, Hong Kong, SAR, 999007, China. [5]These authors contributed equally: Ya Yao, Xinnian Li. ✉e-mail: yaoj@zstu.edu.cn; joselito.razal@polyu.edu.hk; k.usman@deakin.edu.au

Specific challenges in developing MXene-based sensors

What makes MXenes good materials for sensors?. MXenes are highly versatile materials for diverse sensor applications. Their outstanding properties, including high electrical conductivity[34], chemically active surfaces[35], and single-sheet mechanical flexibility[36], meet the critical requirements for effectively responding to various stimuli[37]. For example, their combination of mechanical flexibility and electrical conductivity makes them ideal for pressure and strain sensors used in wearable devices, robotics, and structural health monitoring. MXene-based fibers have been investigated for their responsiveness to external stimuli, such as humidity changes[38,39], due to their surface chemistry and hydrophilicity.

Their tunable 2D structure facilitates rapid ion transport, enabling swift response times and enhanced sensitivity for superior sensing capabilities[40]. This makes them highly preferable in gas sensors for detecting various gases such as NH_3[41,42], CH_4[43,44] and CO_2[45]. MXenes can also be used in electrochemical sensors for detecting a wide variety of chemical species, ranging from pollutants (e.g. pesticides)[46] and heavy metals (e.g. cadmium and lead)[47] to biomarkers (e.g. human anti-ASGPR)[48].

As mentioned above, the versatility of MXenes' chemistry and the variety of structures allow for the development of different sensor types. For simplicity, we categorized these sensors into three groups (Fig. 1):

1. Physical sensors, which rely on structural deformations to change resistivity or capacitance.
2. Chemical/electrochemical sensors, which detect changes in resistance and electrochemical behavior from interactions with the MXene surface.
3. Optical/spectroscopic sensors, which use MXene's optical properties to detect stimuli such as light, chemicals, and biomolecules.

Based on the current literature, we have identified some key challenges associated with the fundamental mechanism and device fabrication processes. These challenges include understanding the underlying principles that govern sensor performance and optimizing fabrication techniques to ensure consistency and scalability.

Common challenges faced by MXene-based sensors and how we can solve them

Physical sensors. Physical sensors detect physical changes in the environment, such as strain, pressure, temperature, or light, and convert them into electrical signals[49], for applications that include healthcare[50], robotics[51], and wearables[52]. MXenes are effective for physical sensors due to their exceptional electrical conductivity[53], charge storage capability[54], and piezoresistive properties[49]. To improve responsiveness to physical changes, MXenes are typically used to modify composites, amplifying signals through their inherent conductivity, enhancing device sensitivity, response time, and stress/strain detection[33]. Notably, $Ti_3C_2T_x$ remains the most conductive MXene reported and is currently the preferred choice for this type of sensor. For this section, we discussed common types of MXene-based physical sensors, such as strain, pressure, acoustic, and temperature sensors, with a comprehensive summary of representative examples in Table 1.

Strain sensors

A strain sensor operates on the change in electrical resistance when a material is subjected to stretching[55,56]. Effective strain sensors must provide a wide working linear range with consistent responses and demonstrate stability over at least 500 loading/unloading cycles to endure dynamic use. The layered structure of MXenes is advantageous in accommodating mechanical deformations while maintaining functionality, with a high gauge factor (GF), the figure of merit for sensitivity, which ensures precise strain detection. The MXene-based sensing behavior mainly relies on the disruption of the interconnected $Ti_3C_2T_x$ flakes when strain is applied, altering the material's overall electrical resistance (Fig. 2a-i)[57,58]. The high conductivity of $Ti_3C_2T_x$ maintained over a wide sensing range allows for higher sensitivity, making MXene-based sensors effective for precise sensing applications, such as heartbeat monitoring[57]. The versatility of sensor design is also possible due to MXene's compatibility with many polymers, which eases its processing into films, aerogels, or fibers[3]. MXenes can be incorporated into fibrous structures (e.g., coated yarns), enhancing stretchability

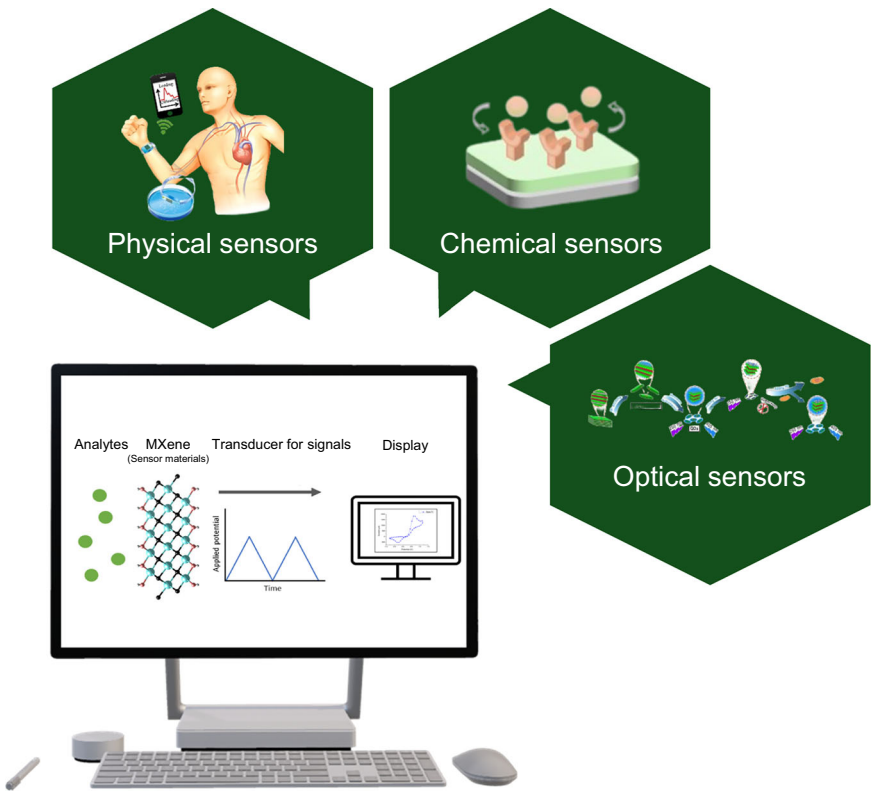

Fig. 1 | A schematic diagram illustrating the types of sensors developed from MXenes. We classify these sensors into three types: (1) physical sensors, (2) chemical/electrochemical sensors, and (3) optical/spectroscopic sensors.

Table 1 | Representative studies on physical sensors, including performance comparisons with existing materials reported in the literature

Type	Material/s	Contains MXene?	MXene load	Sensitivity (S)/gauge factor (GF)	Sensing/ detection range	Response time (ms)	Recovery time	Stability/ load–unload cycles	Ref.
Strain sensors	Graphene–PDMS	No	–	$S = 1875.53\ kPa^{-1}$ (0–20 kPa); 853.2 kPa (20–40 kPa)	0–40 kPa	0.5	0.8 ms	15,000	206
	PEDOT:PSS	No	–	$S = 931.6–770.4\ kPa^{-1}$ (<1.5 kPa); $770.4–51.3\ kPa^{-1}$ (1.5–15 kPa); $51.3–31.9\ kPa^{-1}$ (15–20 kPa)	34 Pa–20 kPa	0.15	–	20,000	207
	CNTs-TPU	No	–	GF = 2.51 (10% strain); 166.7 (350% strain)	10–350%	167	–	10,000	208
	PAM organo-hydrogel	No	–	GF = 98.3 (0–1.5%); 131 (1–40%); 1275 (40–90%)	0.05–90%	147	147 ms	2100	209
	$Ti_3C_2T_x$ MXene/PU fibers	Yes	1–30 wt%	GF = 12,900 (0–152%); 238 (0–50%)	0–152%	–	–	1000	57
	$Ti_3C_2T_x$ MXene/graphene films	Yes	<50%	GF = 1148.2 (52.6–74.1%); 190.8 (0–56.2 %)	0–74.1%	130	–	5000	58
	Spin-coated $Ti_3C_2T_x$ MXene on PU nanofiber mat	Yes	Complete coverage of the fiber mat surface	GF = 228 (0–150%)	58–150%	–	–	3200	59
	Spin-coated $Ti_3C_2T_x$ MXene on PU/PAN nanofiber mat	Yes	Complete coverage of the fiber mat surface	GF = 9.69 (0–80%)	0–80%	<140.6 ms	–	1750	62
	TPU/CNTs@MXene	Yes	10 wt% MWCNTs ($30 \times 5\ mm^2$) soaked in 4 mg mL^{-1} MXene solution.	GF = 13 (0–40%); 73 (40–80%); 363 (80–101%)	0–100%	Real-time	–	200	210
	GnP-MXene coated Poly(styrene–butadienestyrene) nanofiber mat (Cellulose nanocrystals as binder)	Yes	Complete coverage of the fiber mat surface (0–50 wt% of the coating formulation)	FG = 400 (at 100%); 76.1 (at 10%)	0–200%	100 ms	100–120 ms	2000	211
Pressure sensors	PVA/H_3PO_4	No	–	$S = 3302.9\ kPa^{-1}$ (<10 kPa); $671.7\ kPa^{-1}$ (10–100 kPa); $229.9\ kPa^{-1}$ (100–360 kPa)	0.08 Pa–400 kPa	9 ms	18 ms	2000	212
	Graphene	No	–	$S = 229.8\ kPa^{-1}$ (0–0.12 kPa); $26.9\ kPa^{-1}$ (0.4–1 kPa)	0–1 kPa	–	~1084.6 mm s^{-1} (recovery speed)	100,000	213
	$Ti_3C_2T_x$ MXene/r-GO aerogels	Yes	20:1, 10:1, 5:1 MXene: r-GO ratios	$22.56\ kPa^{-1}$	<10 Pa	~200 ms	~200 ms	10,000	66
	$Ti_3C_2T_x$ MXene/poly(vinylidene fluoride-trifluoroethylene) (PVDF-TrFE)	Yes	13 wt%	$0.51\ kPa^{-1}$	1.5 Pa–400 kPa	–	–	10,000 at > 167 kPa	68
	$Ti_3C_2T_x$ MXene-coated cellulose yams	Yes	77 wt%	GF = 6.02 (at 20% compression) $7.67\ kPa^{-1}$	0–20%	35 ms	–	2000	60
	MXene/PU	Yes	MXene colloidal solution was uniformly sprayed on the PU surface until the surface resistance is ~5.0–30.0Ω.	$S = 281.54\ kPa^{-1}$ (0.20–1.70 kPa); $509.8\ kPa^{-1}$ (1.0–5.70 kPa); $66.68\ kPa^{-1}$ (5.70–20.30 kPa)	0.20–20.30 kPa	67.3 ms	44.8 ms	10,000	214
	Ag NWs/Graphene/PANFs	No	–	$S = 134\ kPa^{-1}$ (0–1.5 kPa); $0.7\ kPa^{-1}$ (15–75 kPa)	0–75 kPa	20 ms	–	8000	215
	MXene/Ionic film	Yes	The dried n-WF was immersed in MXene solution (5 mg mL^{-1}) for 10 s and dried at 50 °C repeated 4 times.	$S = 200\ kPa^{-1}$ (<60 kPa); $5000\ kPa^{-1}$ (60–200 kPa); $46{,}730\ kPa^{-1}$ (200–800 kPa); $17{,}148\ kPa^{-1}$ (<1.4 MPa)	20 Pa–1.4 MPa	98 ms	70 ms	10,000	216

Table 1 (continued) | Representative studies on physical sensors, including performance comparisons with existing materials reported in the literature

Type	Material/s	Contains MXene?	MXene load	Sensitivity (S)/gauge factor (GF)	Sensing/ detection range	Response time (ms)	Recovery time	Stability/ load–unload cycles	Ref.
Acoustic sensors	PVDF	No	–	$S = 266\ mV\ Pa^{-1}$	–	–	–	–	217
	Lead-free perovskite	No	–	$S = 150.63\ mV\ Pa^{-1}$; $39.22\ mV\ Pa^{-1}\ cm^{-2}$	100–3000 Hz	–	–	–	218
	Triboelectric nanogenerator (TENG)	No	–	$S = -30 \pm 3$ dB	20–20,000 Hz	Real-time	–	–	219
	Epoxy resin/Al film	No	–	$S = 11.1\ mV\ Pa^{-1}\ mm^{-2}$	15–10,000 Hz	Real-time	–	–	220
	MXene-PDMSP-PE	Yes	The MXene solution was spin-coated on the PDMS-PE substrate.	$S = 62\ kPa^{-1}$	150 Hz–3 kHz	15 ms	25 ms	–	76
	MXene/MoS_2	Yes	0.5 mL MXene (1 mg mL^{-1}) and 0.5 mL MoS_2 (1 mg mL^{-1}) were evenly sprayed on nitrile powder-free gloves.	S = 25.8 mV/dB	40–3000 Hz	4 ms	–	–	78
Temperature Sensors	MXene/PEI	Yes	The optimal MXene concentration (0.8 mg mL^{-1}) was used to prepare the MXene/PEI fibrous network with 1.5 × 1.5 cm^2 size fixed onto a Cu-coated electrode.	S = −5 °C (80 kPa^{-1}) to 150 °C (20 kPa^{-1})	−5 °C (liquid N_2) to 150 °C	163 ms	–	10,000 at RT; 2000 at 100 °C; and 500 at −5 °C	221
	ITO-In_2O_3-Al_2O_3	No	–	S = 129.80 μV/ °C	25–1300 °C	3.52 ms	–	–	222
	Rubber/CNT	No	–	GF = 25.98	30–100 °C	200 ms	–	–	223
	Pt/In_2O_3	No	–	S = 204.35 μV/°C	–	2010 ms	–	–	224
	PEDOT:PSS-PDMS	No	–	$S = 0.042\ °C^{-1}$	30–55 °C	Real-time	–	–	225
	MXene-PDMAEMA	Yes	The MXene-PDMAEMA thin films have varying thicknesses between 20 and 80 μm.	S = 0.8 mS	25–40 °C	–	–	–	80
Photo-sensitive sensors	Ga-doped In_2O_3	No	–	$S = 7.6 \times 10^4$	915–1550 nm	30 ms	10 ms	–	226
	PM6:TPDC-4F	No	–	$D^* = 1.27 \times 10^{13}\ cm\ Hz^{1/2}$ at 800 nm	300–900 nm	6.81 μs	5.41 μs	–	227
	Graphene/PM6:Y6	No	–	$D^* = 1.47 \times 10^{14}$ Jones at 650 nm	488–895 nm	20 μs	8.4 μs	–	228
	Paraffin wax-MXene	Yes	MXene films with thickness of ~6 μm put on a solid PW coated on a glass slide.	$S = 4.6\ m^{-1}/°C$	–	380 ms	–	>20,000	86
	LDPE/MXene	Yes	The MXene dispersion (5 mg mL^{-1}) was uniformly sprayed on the surface of the LDPE film.	$S = 38\ mW\ cm^{-2}$	–	–	–	–	87

D^* = Detectivity

Text in bold refers to sensor materials containing MXene.

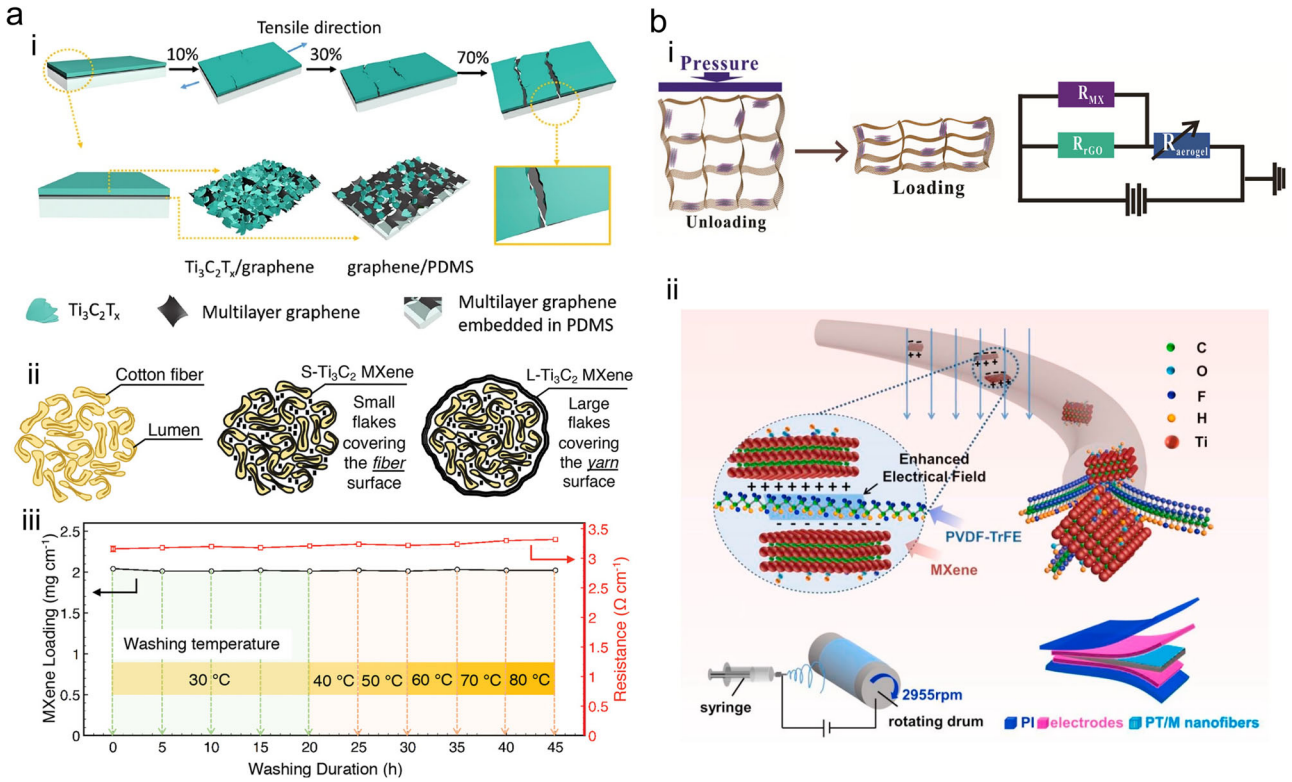

Fig. 2 | Most common types of MXene-based physical sensors: (a) strain and (b) pressure sensors. a-i Strain sensing mechanism via the disruption of interconnected MXene flakes to alter overall electrical conductivity. Reproduced with permission from ref. 58 (copyright American Chemical Society, 2019). **a-ii** Conductive MXene-coated cotton yarns knitted using conventional textile industry-scale equipment. **a-iii** MXene-coated cotton yarns exhibiting minimal resistance increase even after 45 washing cycles. Reproduced with permission from ref. 60 (copyright Wiley VCH, 2019). **b-i** Mechanism for pressure-based sensing where applied force is converted into an electrical signal, reproduced with permission from ref. 60,65 (copyright American Chemical Society, 2018). **b-ii** Enhanced pressure-sensing in MXene-PVDF-TrFE composite nanofibers enabled by MXene-induced piezoelectric coupling in the polymer. Reproduced with permission from ref. 69 (copyright Elsevier, 2021).

and allowing integration into textiles. These sensors have higher strain detection limits and mechanical resilience, making them ideal for wearable devices, robotics, and flexible electronics. For example, Yang et al. developed $Ti_3C_2T_x$ MXene@TPU sensors by spin-coating MXene dispersions onto electrospun thermoplastic polyurethane (TPU) mats, achieving high sensitivity (GF = 228 and LOD = 0.1%), with a working range up to 150% strain[59]. However, for most of these studies, the washability of $Ti_3C_2T_x$, stemming from ineffective coating techniques, remains a limitation, warranting further investigation. The selected fabrication technique, such as spin coating, printing, or layer-by-layer assembly, directly affects film uniformity, adhesion, and strain transfer efficiency between the MXene layer and the substrate. Inconsistent control of these factors can lead to significant variations in sensor output, increased hysteresis, accelerated fatigue, and ultimately, reduced performance and reproducibility across batches.

To address coating issues and improve material utility, methods focusing on substrate compatibility and optimized $Ti_3C_2T_x$ integration have been explored. The work of Uzun et al.[60] demonstrated that highly conductive MXene-coated cotton yarns can be knitted with equipment used in the textile industry (Fig. 2a-ii). After 45 cycles of washing, the MXene-coated cotton yarns showed only a minimal increase in resistance (Fig. 2a-iii), attributed to the strong H-bonding of the cellulose-rich fibers with MXene. Sensor performance can be further improved by chemically modifying the interaction between MXene and substrates, which is advantageous for non-fibrous architectures[61], which typically have fewer anchor points for MXenes. For instance, an interface binder such as polyacrylonitrile (PAN) can enhance the interaction of MXene with a TPU substrate during electrospinning. The resulting MXene/TPU/PAN strain sensor achieved a wide sensing range of 0–80%, GF of 9.69, LOD of <0.1%, and durability after >1750 cycles[62]. Flexible substrates such as TPU or polydimethylsiloxane (PDMS) can also be layered with MXenes to extend the strain detection range while maintaining high conductivity, enabling sensors to withstand larger deformations. Seyedin et al. demonstrated the continuous fabrication of wet-spun MXene/PU coaxial fibers, which are both highly conductive and stretchable. These fibers, featuring an MXene/PU core surrounded by a flexible PU sheath, exhibited a low percolation threshold of ~1 wt% MXene and outstanding strain sensing capabilities, with a GF of ~12,900 at 152% strain. This coaxial design also enhanced the fibers' stability under cyclic deformation[57].

It is important to note that the amount of MXene incorporated critically affects the percolation network and gauge factor. Insufficient MXene loading can result in poor conductivity and low signal-to-noise ratios, while excessive loading may reduce sensitivity due to limited strain-induced resistance changes.

Other 2D materials, such as graphene, can also be integrated to enhance the strain sensing performance of MXene sensors (Table 1)[63,64]. In the study by Taromsari et al., a graphene nanoplatelet (GnP)–MXene hybrid was used to form a strain sensor with enhanced strain sensitivity (GF ~ 400 at 100% strain) and cyclic stability after over 2000 cycles.

Pressure sensors

A pressure sensor generally consists of a force-sensitive layer, conductive electrodes, and a flexible substrate that works by converting the physical force exerted by pressure into an electrical signal[52]. MXene-based pressure sensors use piezoresistive, piezoelectric, capacitive, triboelectric, and potentiometric properties, causing electrical resistance variations under pressure (Fig. 2b-i)[65].

In piezoresistive sensors, MXene is used as a force-sensing layer, with its conductivity changing in response to external pressure. An example is the

piezoresistive sensor built by Ma and co-workers using an ultralight and superelastic MXene/reduced graphene oxide (MX/rGO) hybrid 3D aerogel with exceptionally high sensitivity (22.56 kPa^{-1}), rapid response time (<200 ms), and excellent stability over 10,000 cycles[66]. Meanwhile, a capacitive pressure sensor (CPS) detects the change in capacitance from the altered separation distance between two parallel electrodes[67]. The development of CPS devices faces difficulties in achieving both optimum mechanical properties and high sensitivity. An example of a study addressing this challenge is the work by Sharma et al., which demonstrated the fabrication of a wearable CPS utilizing a MXene ($Ti_3C_2T_x$)/poly(vinylidene fluoride–trifluoroethylene) (PVDF–TrFE) composite scaffold as the dielectric layer to enhance LOD (1.5 Pa), pressure range (up to 400 kPa), and mechanical stability for over 10,000 cycles under high pressure (~167 kPa)[68]. Similar challenges are also common for piezoelectric sensors. In the study by Wang et al., MXene's non-centrosymmetric lattice was utilized to enable charge polarization under external force, generating a piezoelectric effect, which was further enhanced by the piezoelectric properties of PVDF-TrFE. PVDF-TrFE/MXene composite nanofibers developed using electrospinning exhibited improved piezoelectric performance, with a peak-to-peak output voltage of 1.58 V (three times higher than pure PVDF-TrFE), a linear pressure response, and an energy harvesting capability of ~3.64 mW/m^2 (Fig. 2b-ii)[69]. For triboelectric sensors, difficulties in satisfying high dielectric constant, large electron affinity, and surface area to improve charge density were mitigated by using MXene as an electrode material. This was demonstrated in the development of a triboelectric nanogenerator (TENG) using MXene, carboxylic acid-functionalized single-walled carbon nanotubes, and a fluorinated polymer matrix, performing at an outstanding output voltage of ~300 V, current of ~40 μA under 20 N force, and 92% charge retention after 1 h. Its superior durability and mechanical stability enabled it to power wearable electronics and support a wearable pH monitoring system[70,71]. Lastly, potentiometric sensors utilize MXene's flexibility and functional groups for redox reactions, providing self-powered, stable electrical signals without the need for external energy sources, ideal for miniaturized electronic skin[71].

Another critical factor in integrating MXene into pressure sensors is selecting an optimal microstructure for the force-sensitive layer to enhance performance. To improve the pressure detection range and sensitivity, MXene is incorporated into porous structures (e.g., aerogels and foams) to increase the surface area for conductive pathways. Recent developments include the fabrication of a compressible, lamellar aerogel by combining MXene nanosheets with cellulose nanocrystals (CNCs) to prevent restacking during fabrication. The stable lamellar structure ensures elasticity and stable signal response under pressure, making it ideal for wearable piezoresistive devices and biosignal detection[72]. MXene-based fibers and fabrics can also improve the interaction between the force-sensitive and electrode layers, enhancing response speed and sensitivity. As example, a wearable, washable pressure-sensing fabric was created by utilizing the natural roughness of cotton fibers and MXene's functional groups to achieve strong interfacial interactions. The MXene-coated fabric showed high pressure sensitivity (gauge factor of 7.67 kPa^{-1}), fast response (<35 ms), and long-term durability (>2000 cycles), and was demonstrated as a flexible human–machine interface with multitouch capabilities and rapid response times[73]. These techniques enable MXene sensors to achieve high sensitivity, fast response, and long-lasting durability due to the capability to produce structures with optimized electrical conductivity and mechanical flexibility.

However, MXene's pressure-sensing capabilities also lag those of other composites. For instance, rGO/PET-based fiber sensors were found to outperform their MXene/PET counterparts due to the limitations of MXenes discussed in the previous sections[74]. Modifications to its structure or integration with supporting materials could enhance performance and expand its applications.

Acoustic sensors

Acoustic sensors detect sound or vibrations and convert them into electrical signals. Selecting materials with high conductivity and piezoelectric characteristics is key to efficient signal conversion. Flexibility and compatibility with various surfaces that maximize sound adsorption further enhance their application potential. Moreover, suitability for compact designs is essential for seamless integration into portable or wearable devices[75].

Prominent MXene-based acoustic sensors include a highly sensitive artificial eardrum using double-layer films of MXene, PDMS, and poly(-ethylene) (PE) (Fig. 3a-i)[76]. MXene nanoflakes were evenly distributed within a pyramid-shaped PDMS structure, leveraging two enhancements: the large interlayer spacing in the MXene layer and the PDMS micropyramid design (Fig. 3a-ii). This sensor demonstrated high sensitivity (62 kPa^{-1}), low-pressure detection (0.1 Pa), and a working frequency range of 0.15–3 kHz, showcasing its potential for wearable human–machine interaction devices. These advancements in MXene acoustic sensors show promise for speech recognition applications.

However, refinement is needed to enhance their frequency response and detection limits for more effective human voice sensing[75]. MXenes have low sensitivity at low pressures and a limited frequency range due to their inherent stiffness and excessive electrical conductivity, which hinder their ability to detect small pressure changes and high-frequency sound waves effectively[77]. Hybrid assemblies of MXenes and transition metal dichalcogenides (TMDs) address key limitations of MXenes as acoustic sensors. The piezoresistive properties and chemical stability of TMDs improve the sensor's robustness, durability, and frequency range. This synergy enhances sensitivity, enabling more accurate detection of sound across a wider range of frequencies, making the hybrid structures ideal for applications like voice recognition and environmental monitoring. In a study by Chen et al., they developed a machine-learning-based speech recognition system using flexible MXene/MoS_2-coated plastic substrates[78]. The combination of flexible substrate and nanomaterial hybrid enhances mechanical strength, enabling the composite to vibrate with sound, alter resistance, and distinguish sound frequencies and volumes.

Temperature sensors

Temperature sensors detect changes by converting thermal energy into electrical signals. MXenes, especially $Ti_3C_2T_x$, are favored for this type of sensor due to their excellent electro-thermal and photo-thermal conversion capabilities in sensor design[79]. However, due to MXene's high electrical conductivity, the resistivity does not change significantly with temperature, requiring additional treatments for enhancing temperature sensitivity. To address this, Tran et al. formulated a composite of MXenes and poly(2-(dimethylamino) ethyl methacrylate) (PDMAEMA)[80]. As the temperature decreases, PDMAEMA aligns perpendicularly to the substrate, increasing the spacing between MXene flakes and reducing conductivity. This resulted in an MXene composite with a conductivity that responds more significantly than pure MXene to temperature shifts between 25 and 40 °C[21,81]. Cao et al. also fabricated a temperature sensor using an MXene and PDMS substrate hybrid. When heated, the PDMS substrate swells, causing the MXene flakes to disrupt the percolation network, leading to a significant increase in the MXene resistance[82].

Significant progress in this area has focused on solving mechanical instability during repeated temperature-response cycles, as swelling or realignment of polymers and additives can damage the sensing architecture. These issues were mitigated by using temperature-stable polymers and robust structures for support. Zhao et al. developed a tissue-like sodium alginate hydrogel-based temperature sensor that operates across a wide temperature range (−20 to 100 °C), with the MXene providing conductivity and thermal responsiveness, while the SA-coating layer enhances heat sensitivity (Fig. 3b)[83]. In a recent study, Fu et al. designed MXene fiber artificial muscles (MFAMs) with tensile actuation capabilities upon heating. As the temperature increases from 25 to 125 °C, the intra-sheet spacing of MXene decreases, resulting in a reversible muscle contraction of up to 21.0%[84]. These advancements highlight MXenes' potential for high-performance temperature sensors, leveraging their thermoelectric properties, flexibility, and conductivity.

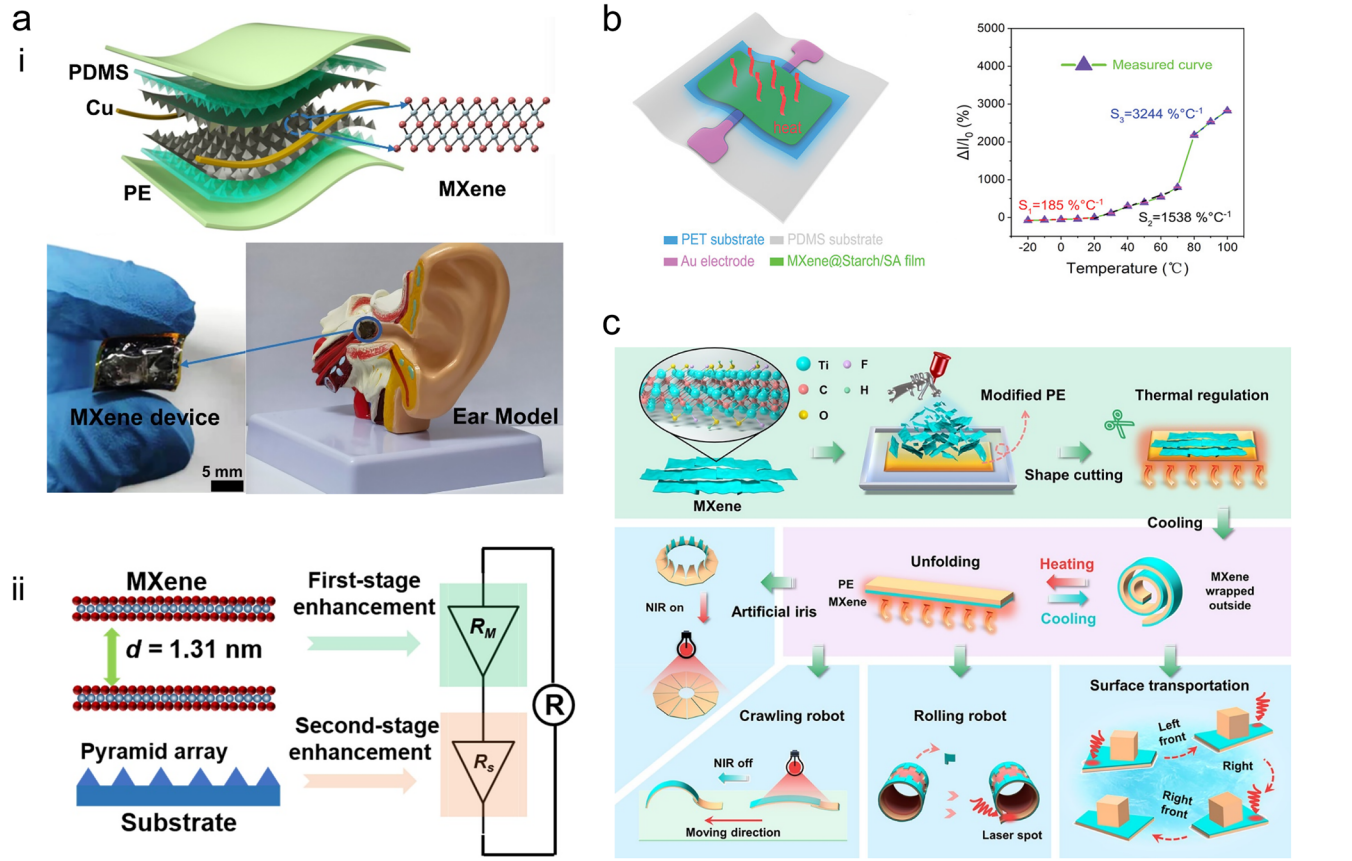

Fig. 3 | Force-sensitive types of physical sensors based on MXenes, such as acoustic, temperature and photosensitive sensors. a-i Artificial eardrum using double-layer films of MXene, PDMS, and PE. **a-ii** Distribution of MXene in pyramid-shaped PDMS, leveraging enhancements in interlayer spacing and micro-pyramid design. Reproduced with permission from ref. 76 (copyright The American Association for the Advancement of Science, 2022). **b** Composite films of MXenes and PDMAEMA as temperature-sensitive sensors. Reproduced with permission from ref. 80 (copyright Wiley VCH, 2022). **c** Films consisting of symmetrically distributed PW and MXene layers bending under intense sunlight and stretching under normal light conditions. Reproduced with permission from ref. 86 (copyright American Chemical Society, 2021).

Photo-sensitive sensors

MXene-based photosensors use the properties of MXene to interact with light, triggering structural changes. An early example is Chertopalov's work using partially oxidized MXene as a photo-responsive material. Here, the spontaneous oxidation of MXene thin films produces $Ti_3C_2T_x$–TiO_2 composites with resistance that can vary upon UV irradiation[85]. Although MXenes generate heat from absorbed light, the architecture lacks significant resistance changes with temperature, requiring additional treatments for enhanced sensitivity. In the study of Xiao et al., they presented a flexible actuator composed of paraffin wax (PW) and a $Ti_3C_2T_x$-rich layer. As MXene photothermally facilitates the evaporation of adsorbed moisture within the layers, the asymmetric distribution of the hydrophobic (PW) and hydrophilic (MXene) components causes an uneven change in *d*-spacing, making the film bend under intense sunlight and stretch under normal light conditions, enabling inchworm-inspired crawling motion (Fig. 3c)[86]. Similarly, a study by Luo et al. demonstrated a bilayer actuator by spraying MXenes onto a plasma-treated LDPE film[87]. These modification approaches have opened a new generation of MXene-based actuators for soft robotics and wearable devices with adaptive structures.

Chemical sensors. Chemical sensors, including chemiresistive, chemicapacitive, and electrochemical sensors, convert signals arising from chemical interactions between the sensor material and an analyte into analytical signals that are correlated with the amount of analyte interacting with the material surface. Generally, these sensors experience a change in impedance when an analyte binds to the surface, expressed as higher or lower resistance, voltage, or current. The majority are used as biosensors for analytes like biomolecules[88,89] and biomarkers[90–92], as MXene under certain conditions has also shown exceptional biocompatibility[93,94]. Additionally, MXenes possess a unique combination of metallic-like conductivity and highly reactive surface terminations, which enhances bremains uncertain due to a lack of extended experimental dataoth charge transport and interactions with target analytes. The diverse interactions of MXenes with chemical species have enabled the development of various sensors. This section summarizes (Table 2) and highlights three key types of MXene-based chemical sensors and their associated challenges.

Chemiresistive sensors

Chemiresistive sensors measure variations in electrical resistance brought about by analyte adsorption on the sensor surface, altering charge carrier density[95,96]. Due to the simple and indiscriminate nature of the mechanism, chemiresistive sensors are ideal for applications requiring high adsorption and response rates, like gas sensing. Materials with reactive or porous surfaces capable of high signal-to-noise (S/N) output, including metal oxides[97,98], carbon nanomaterials[99–101], and conducting polymers[102], have found success in the field but suffer from high operating temperatures, low processability, and declined performance when bent or twisted[103,104]. MXene overcomes these issues through its mechanical properties, processability, and thermal stability. Early reports of MXene-based chemiresistors focused on the detection of volatile organic compounds (VOCs) like acetone, ethanol, ammonia, and propanal using $Ti_3C_2T_x$[95,96], which exhibited an S/N ratio more than two orders of magnitude higher than other 2D materials[105] (Fig. 4a-i). DFT simulations highlighted that the hydroxyl (–OH) surface

https://doi.org/10.1038/s43246-025-00907-y

Table 2 | Representative studies on chemical sensors, including performance comparisons with materials reported in the literature

Type	Material	Analyte	Contains MXene?	MXene load	Linear range	LOD/sensitivity	Response/ recovery time	Stability	Notes	Ref.
Chemiresistive	CuO NSs + CeO_2 NPs	NO_2 gas (100 °C)	No	–	200 ppb–600 ppt	600 ppt	15 s to 10 ppm NO_2	30 days	Also demonstrated that the sensor operates at 100 °C	229
	Pd-SnO_2 NPs	Toluene	No	–	1–10 ppb	200 ppt (initial resistance curve)	Not specified	Not specified	2 sensing mechanisms based on the pulse	230
	PEDOT:PSS/TiO_2/ZnO NWs	H_2	No	–	1–20 ppm	9 ppt at 50 °C, 1 ppb at 25 °C	65 s to 100 ppb H_2	9 months	Flexible sensor, works even at 50 °C	231
	$Ti_3C_2T_x$ MXene film (vacuum-dried) w/Au contacts	**VOC gases: acetone, ethanol, ammonia, and propanal, NO_2, SO_2, CO_2**	**Yes**	**Not specified (>400 mg)**	**Not specified**	**50–100 ppb at RT**	**Not specified**	**Not specified**		95
	MXene	**Microcystin-LR in water from cyanobacteria *Microcystis aerouginosa***	**Yes**	**0.025 mg (thin coating only)**	**1–104 ng L^{-1}**	**0.18 ng L^{-1}**				232
	MXene	$W_{18}O_{49}$ NRs/$Ti_3C_2T_x$ MXene nanocomposites	**Yes**	**2 wt% MXene**	**0.17–500 ppm**	**170 ppb**	**5.6 s/6 s**	**Tested for 100 cycles**		96
Capacitive	GO	RH	No	–	40–99% RH	8504% (C/Co) at 500 Hz	170/40 s	15 days		233
	MWCNT	RH	No	–	10–90% RH	~1480% ($\Delta C/C0$)	0.8/0.78 s	48 h/2 days		234
	ZrP nanoplates	RH	No	–	10.9 to 91.5% RH	2409 (C/Co) @ 100 Hz	x/9 s	4 wk		235
	MXene-decorated flower-like SnS_2, in situ hydrothermal	**RH**	**Yes**	**30 wt% MXene**	**7–93% RH**	**433,827.42% (△C/Co) at 1 kHz**	**22.5 s/0.21 s**	**15 days**		121
	Ti_3C_2/Ag hybrid on PDDA substrate	**RH**	**Yes**	**98 wt% MXene (2 wt% Ag)**	**35–95% RH**	**106,800% (△C/Co)**	**80/120 ms**	**40 days**		122
Electrochemical	SFB-imprinted poly-methyldopa on PGE	Sofosbuvir	No	–	10–0.1 pM	0.031 pM	30 s	3 days	RSA on plasma & (pharmaceutical) tablet samples	236
	ENR-imprinted APTES-based polymer on MWCNT on GCE	Enrofloxacin	No	–	2.8 pM to 28 µM	0.9 pM	Not specified	7 days	RSA on seawater samples	237
	Cortisol-specific antibodies on SnO_2 nanoflake-integrated conductive carbon fiber (SnO_2/CCY)	Cortisol	No	–	10 fg mL^{-1} to 1 µg mL^{-1}	1.6 fg mL^{-1}	Not specified	1 month	Indirect sensing using ferrocyanide probe; RSA on sweat	238
	Pt/MoS_2/Ti_3C_2 MXene on GCE	**Methyl parathion, chlorpyrifos, dimethoate**	**Yes**	**Not specified (~1/3 of composite load)**	**1 pM–1 µM**	**0.471 pM**	**Not specified**	**7 days**	**RSA on fruits & veggies**	239
	Cortisol-imprinted poPD on MXene/graphene composite	**Cortisol**	**Yes**	**33 wt% MXene in the MXene/ graphene composite**	**1 fM–10 µM**	**0.4 fM**	**Not specified**	**1 month**	**RSA on saliva**	240
	DNA nanostructure/ MXene nanocomplexes	**Gliotoxin**	**Yes**	**10 vol% MXene**	**5 pM–10 nM**	**5 pM**	Not specified	**Not studied**		241

Text in bold refers to sensor materials containing MXene.

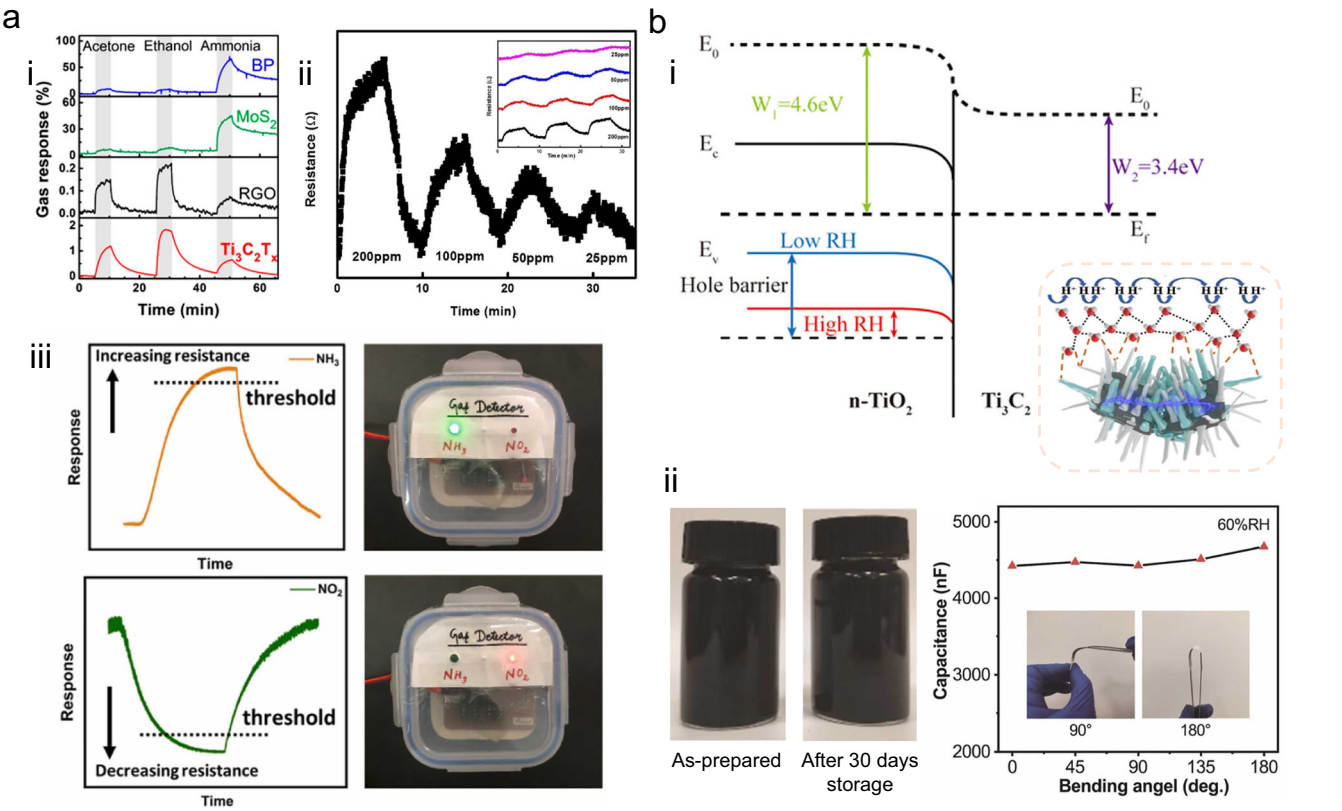

Fig. 4 | MXene-based chemically responsive sensors, such as chemiresistive and capacitive sensors. a-i MXene-based chemiresistors focused on the detection of VOCs using $Ti_3C_2T_x$. Reproduced with permission from ref. 105 (copyright American Chemical Society, 2018). **a-ii** Acetone sensing performance of a $Ti_3C_2T_x$ chemiresistive sensor with p-type behaviour. Reproduced with permission from ref. 106,107 (copyright American Chemical Society, 2017). **a-iii** Tuned selectivity between two gases exhibited by $Ti_3C_2T_x/WS_2$ heterostructure, at which reducing and oxidizing gases produced opposite transient response curves. Reproduced with permission from ref. 107 (copyright Elsevier, 2023). **b-i** Ti_3C_2/TiO_2-based humidity sensor demonstrating water-induced carrier concentration and lowered hole energy level barrier, resulting in increased conductance. Reproduced with permission from ref. 120 (copyright American Chemical Society, 2019). **b-ii** Stable SA/MXene ink used for printing flexible humidity sensors even after storage for 30 days. Reproduced with permission from ref. 124 (copyright Elsevier, 2022).

group largely improves affinity to analytes through strong hydrogen-bonding interactions[106]. The specific mechanism for chemiresistive sensing in $Ti_3C_2T_x$ is similar to that of p-type materials, where the adsorption of reducing gas molecules in defect sites and surface functional groups leads to an increase in resistance[106,107] (Fig. 4a-ii). Theoretical simulations suggested that introducing additional vacancies in Ti coordination could further enhance sensing performance by increasing the physical adsorption of analytes[108]. The findings from these pioneering studies, including the sensing mechanism of $Ti_3C_2T_x$, opened opportunities in developing similar technologies based on other MXene variants, such as $V_4C_3T_x$ and V_2CT_x[102,109]. Interestingly, the vanadium (V)-based MXenes were found to respond to nonpolar gases as well. V_2CT_x-based gas sensors can detect hydrogen and methane with LODs of 2 and 25 ppm, respectively, at room temperature, ascribed to the high affinity of gases to the transition metal V[102]. Aside from typical VOCs, chemiresistive MXene-based sensors are also popular in humidity sensing due to MXene's hydrophilicity[110–113].

Achieving higher sensitivity with pristine MXene-based chemiresistive sensors encounters issues such as sheet restacking. For example, fabrication techniques like drop-casting or vacuum filtration can create dense MXene membranes and block active sites. This can be addressed by using porous architectures or modified 3D templates to enhance mass transport. $Ti_3C_2T_x$-coated porous nonwoven fabric gas sensor enhanced analyte diffusion and interaction with MXene, achieving a response 3.5 times greater than the as-prepared MXene at a fast rate (1.5 min) with low LOD (50 ppb)[114].

MXene can be hybridized with inorganic nanomaterials[115,116] or organic fillers[117] to increase active sites and/or reduce or modulate its electrical conductivity, enabling the measurement of smaller resistance changes. For instance, $Ti_3C_2T_x/WSe_2$ heterostructure gas sensors exhibited higher sensitivity and faster recovery time than $Ti_3C_2T_x$ after exposure to ethanol (1–40 ppm). Aside from the stark difference in performance, the two samples exhibited contrasting sensing mechanisms, with $Ti_3C_2T_x$ as p-type and $Ti_3C_2T_x/WSe_2$ as n-type sensors[115]. Control over band structures was used to improve selectivity between two gases, resolving the issue of indiscriminate sensing in chemiresistive sensors, using a $Ti_3C_2T_x/WSe_2$ heterostructure[107], whereby reducing and oxidizing gases produced opposite transient response curves (Fig. 4a-iii). Hybrid materials can also enable the detection of species such as biomolecules. MXene-chitosan sensors fabricated via dip coating with chitosan are used as enzymatic biosensors. Chitosan and $Ti_3C_2T_x$ served as a support matrix to immobilize cholesterol oxidase enzymes and enhance electrical conductivity[117].

Capacitive sensors

MXene's hydrophilicity makes it ideal for capacitive humidity sensing, measuring capacitance changes due to changes in electrode distance or area. Although its potential for humidity sensing was implied in early reports[111,118], pristine MXene suffers from poor selectivity and sensitivity[119]. This issue is remedied by employing semiconductors to design heterostructures and form Schottky barriers. The Ti_3C_2/TiO_2-based humidity sensor was prepared by growing TiO_2 nanowires on exposed Ti sites across the $Ti_3C_2T_x$ structure, increasing the surface area and adsorption sites to enhance the sensor performance. Water adsorption increased carrier concentration and lowered the hole energy level barrier at the Ti_3C_2/TiO_2 Schottky junction, increasing conductance and achieving high sensitivity (280 pF/RH%) even at low humidity[120] (Fig. 4b-i). Similarly, high surface

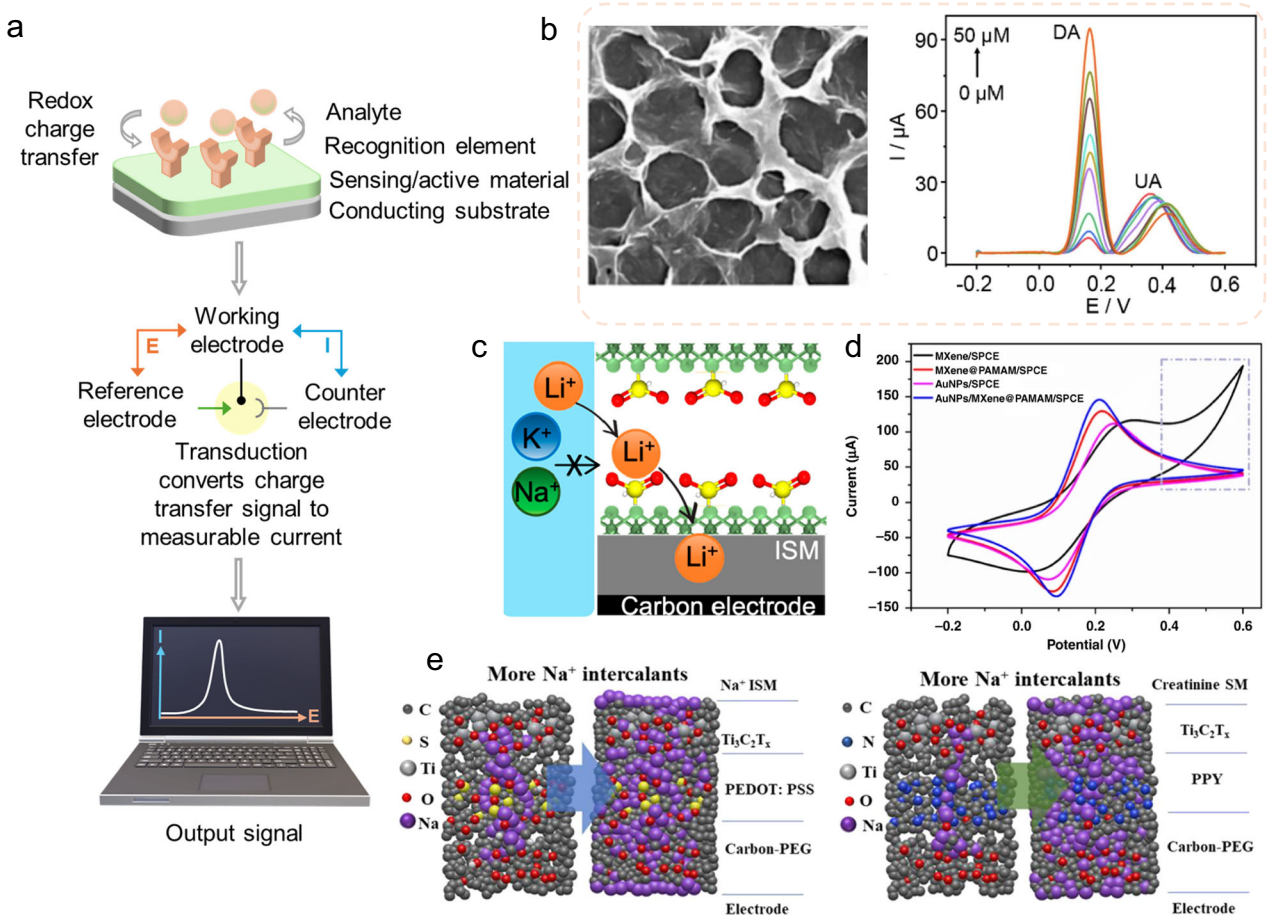

Fig. 5 | MXenes as platform for electrochemical sensors. a Redox-mediated charge transfer generates a current or potential proportional to analyte interaction. **b** Enhancement of sensing performance by controlling electrode porosity. Reproduced with permission from ref. 147 (copyright Elsevier, 2023). **c** Inherent layering of MXene as an ideal structure for ion-selective electrodes. Reproduced with permission from ref. 145 (copyright American Chemical Society, 2023). **d** Growing poly(amidoamine) dendrimers to improve anodic stability of $Ti_3C_2T_x$. Reproduced with permission from ref. 151 (copyright Springer Nature, 2022). **e** Sensing efficiency improved by adding sodiated nanoporous carbon/PEG, $Ti_3C_2T_x$, and PEDOT:PSS layers for Na^+ and creatinine detection. Reproduced with permission from ref. 155 (copyright American Chemical Society, 2023).

area tin sulfide (SnS_2) was decorated with $Ti_3C_2T_x$ sheets to achieve a capacitance increase (sensitivity metric) of 433,827% from 7% to 93% RH at 1 kHz excitation frequency, compared to the 59,306% increase using just SnS_2[121]. Apart from MXene-semiconductor heterostructures, using MXene with metal nanoparticles like silver (AgNPs) also improves charge mobility and sensitivity. $Ti_3C_2T_x$ accommodates two layers of H_2O molecules through H-bonding before succeeding layers are merely physisorbed and become mobile, with some molecules undergoing ionization and therefore acting as charge carriers. The presence of AgNPs decreases the energy barrier for the interaction of water molecules with the sensing layer. The synergy between $Ti_3C_2T_x$ and AgNPs resulted in a 15-fold improvement in sensitivity in the composite sensor (106,800%) vs. $Ti_3C_2T_x$[122]. Furthermore, the interaction between the Ti_3C_2/Ag system can be improved through plasma treatment[123].

MXene's susceptibility to oxidation in aqueous and humid environments affects the integrity and reproducibility, requiring the addition of hydrophobic or antioxidative materials and other post-treatments. For example, a sodium ascorbate (SA)/MXene ink remained stable for printing flexible humidity sensors when stored for 30 days[124] (Fig. 4b-ii). The cross-linked $Ti_3C_2T_x$ film with polyethyleneimine and glutaraldehyde also exhibited improved stability after long-term storage[125].

Electrochemical sensors

Electrochemical sensors rely on redox-mediated charge transfer processes occurring between the material and the analyte to produce a current or potential that is proportional to the amount of analyte interacting with the recognition element (Fig. 5a)[126]. Depending on the technique (potentiometric, amperometric, or impedimetric), sensor design, and electrochemical activity of the analyte, the sensor responds to the analyte either directly or indirectly[127]. These variables play into the adaptability of electrochemical sensing, from material design to technique optimization, and open it up to a wide range of analytes from metal ions to pathogens[128–131] while employing metal-organic frameworks[132,133], enzymes[134–137], aptamers[138,139], and molecularly imprinted polymers[140–142] as recognition elements. MXene's tunable composition, surface reactivity, high conductivity, and large surface area collectively benefit electrochemical sensors[143,144]. For example, the layered structure and surface chemistry of $Ti_3C_2T_x$ are ideal for ion-selective electrodes (ISE) (Fig. 5c), and modification with certain chemical moieties improves selectivity[126,145,146]. Pristine MXene ($Ti_3C_2T_x$) was also found to improve peak separation and sensitivity in multicomponent sensing[88]. Aside from its chemical and electrical properties, architecture and morphology also play a crucial role in the performance of MXene-based electrochemical sensors by optimizing ion mobility within the structure. Controlling the porosity and sheet alignment facilitates the migration of analytes[19,147] (Fig. 5b) and even sensing elements like enzymes[148] into the MXene structure.

The applicability of MXene-based electrochemical sensors is challenged primarily by oxidation in water, which limits their anodic potential windows in aqueous solutions[149,150]. Growing a poly(amidoamine) dendrimer improves the anodic stability of $Ti_3C_2T_x$[151] (Fig. 5d), but the

mechanism by which this occurs remains underexplored. Another relevant issue is the optimization of faradaic interactions between MXene and the analyte, especially at bulk configurations. Noriega et al. reported that thin MXene films composed of large sheets provide better S/N ratio, as opposed to thick films or films made from small sheets[152].

Sheet restacking in electrochemical sensors also limits mass transport. Incorporating spacers with high analyte affinity increases interlayer spacing, creating more active sites for small organic molecules[153,154]. Incorporating MXenes into porous and 3D architectures can also help to further address this issue[155]. Kalasin et al. reported improved sensing efficiency by adding solid-contact sodium (Na^+)-intercalated (sodiated) nanoporous carbon/polyethylene glycol and $Ti_3C_2T_x$ layers to sodiated transducers composed of PEDOT:PSS for potentiometric Na^+ sensing and polypyrrole for voltametric creatinine detection[155] (Fig. 5e).

Optical and spectroscopic sensors. MXene-based optical sensors utilize plasmonic properties and tunable electronic structures to detect stimuli such as light, chemicals, and biomolecules, enabling efficient signal transduction through high conductivity and surface functional groups. MXenes enhance the sensitivity of optical sensors by facilitating strong light–matter interactions and supporting localized surface plasmon resonance (LSPR)[156]. Each type of sensor, along with its associated challenges, is discussed in this section with a comprehensive summary in Table 3.

Plasmonic sensors

Surface plasmon resonance (SPR) occurs when free electrons on a metal surface resonate with incident light. SPR sensors detect molecular interactions by measuring refractive index changes near a metal–dielectric interface. MXene offers significant advantages in SPR sensors due to its large lateral size, which enhances contact with metal layers and facilitates interaction with the sensing medium and electromagnetic fields. Its strong light absorption[157] and low transmission loss[158] improve sensor sensitivity and electric field enhancement near the sensing medium. MXene's optical transparency, stability, and tunable bandgap also enable high penetration depth and sensitivity[159]. Moreover, MXene's high surface area-to-volume ratio enhances the binding capacity of the metal layer for analytes, overcoming the limitations of traditional metal films. Its tunable surface chemistry further underscores its suitability for SPR-based biosensors[160]. It also protects the metal layer from oxidation by acting as a dielectric layer, further boosting sensitivity.

MXene-based SPR sensors are typically fabricated so that incident light interacts with the sensor chip through a prism positioned beneath the sensor substrate. The two most commonly used prism configurations are the Kretschmann and the Otto configurations[161]. In the Kretschmann configuration, light passes through the prism and reflects off a thin metal layer coated on its surface, exciting surface plasmons at a specific resonance angle. In contrast, the Otto configuration features a small air gap between the prism and the metal layer, where surface plasmons are excited by an evanescent wave.

To overcome challenges such as limited penetration depth and sensitivity, advanced designs like a nearly guided wave SPR configuration have been introduced. The Otto setup offers greater durability under high-intensity light due to its superior thermal resistance and reduced wear on the metal layer. However, it is more complex to implement, as it requires precise control of the air gap.

The Kretschmann configuration, on the other hand, is simpler to set up and is therefore preferred for standard applications involving moderate light intensity[162]. MXene's exceptional mechanical and thermal stability[163] makes it particularly well-suited for use in the Kretschmann configuration, further enhancing the performance and practicality of MXene-based SPR sensors.

Multi-pronged factors, such as penetration depth, are crucial for SPR sensors, as they define how far the plasmonic (electric) field extends from the metal surface into the sensing region, determining the interaction range with the target material. In propagating SPR, however, the penetration depth is relatively limited[164]. To address this, researchers have explored various advanced SPR configurations, such as incorporating a thin high-index dielectric film between the metal and sensing layer, known as nearly guided wave SPR, which enhances sensitivity[165].

For example, Wu et al. demonstrated an SPR biosensor enhanced with a few-layer $Ti_3C_2T_x$ MXene, which improves sensitivity and acts as a protective layer on metal thin films. Sensitivity enhancements of up to 46.3% and a maximum of 224.5°/RIU demonstrate the potential use of MXene in advancing SPR biosensing technology[166]. Similarly, a functionalized MXene-based SPR sensor for early SARS-CoV-2 detection by immobilizing thiol-tethered ssDNA on the MXene layer, demonstrating high sensitivity and selectivity[167].

The performance of the proposed SPR biosensor strongly depends on the number of $Ti_3C_2T_x$ MXene layers. Increasing the layer count broadens the Au-based SPR curves due to electron energy loss and shifts the resonance angle through enhanced light absorption. Sensitivity improves significantly up to four MXene layers but tends to plateau beyond that, even when combined with other materials. For example, SPR sensors paired with gold, aluminum, and copper show limited sensitivity gains at $\lambda = 633$ nm, with enhancements of 28.4%, 46.3%, and 33.6% enhancements for 7, 12, and 9 MXene layers, respectively[166].

A theoretical study using finite difference time domain (FDTD) simulations examined MXene layer thickness ranging from 1 to 10 layers and found that thickness significantly affects sensor sensitivity. Notably, the effect varies with surface termination. F-terminated MXene achieved the highest sensitivity at 133.39°/RIU[168].

Although direct experimental research on surface terminations in SPR sensors is still lacking, surface terminations are known to influence MXene's electronic structure. For example, outermost halogen terminations like -I, and -Br can gain electrons and convert to their elemental forms when used as cathodes in $Ti_3C_2I_2$ or $Ti_3C_2Br_2$[169]. This electronic transformation impacts the plasmonic properties of MXene[170,171]. Future experimental studies are expected to further explore how surface terminations affect SPR sensor performance, offering deeper insights into optimizing these materials.

Surface-enhanced Raman spectroscopic (SERS) sensors, another type of plasmonic sensor, amplify weak Raman scattering signals through surface-enhanced scattering. Since the first report of pristine $Ti_3C_2T_x$ MXene as a SERS substrate in 2017[172], numerous studies have explored its properties and applications. Researchers have examined the effects of MXene terminal groups[173], layer thickness[174], and crystallinity[175] on SERS performance.

For instance, $Ti_3C_2O_2$-terminated MXene demonstrates superior SERS activity compared to $Ti_3C_2(OH)_2$ due to its ability to generate a stronger near-field effect. The layer thickness of $Ti_3C_2T_x$ nanosheets also plays a crucial role, as Raman enhancement is highly thickness dependent. Studies have demonstrated that films thinner than 0.8 μm (for 532 nm) and 1.0 μm (for 633 nm) laser excitations provide strong enhancement for methylene blue detection. However, once the thickness exceeds 2.0 μm, the enhancement levels off, indicating a threshold beyond which additional layers no longer contribute significantly to the collective effect. Additionally, crystallinity is key to SERS performance. For instance, a highly crystalline monolayer $Ti_3C_2T_x$ capable of maintaining its structure forms a nucleus-free 2D electron gas, enabling strong visible-range localized SPR (LSPR, defined as the SPR phenomenon exhibited in nano-regime) that enhances SERS sensitivity. Beyond studies of pristine MXene substrates, integrating MXenes with noble metals has emerged as a promising strategy for enhancing SERS performance[176,177]. This approach leverages the plasmonic properties of noble metals alongside the unique electronic properties of MXenes, resulting in highly sensitive and versatile SERS platforms.

A prominent resonance around ~1.7 eV has become a key in understanding the signal enhancement mechanism, though its exact origin remains under investigation[172178]. In the case of $Ti_3C_2T_x$, the near-infrared absorption peak at ~1.7 eV (800 nm) has been attributed to a combination of interband transitions (IBT) and localized surface plasmon resonance

Table 3 | Representative studies on optical sensors, including a comparative analysis of their performance against materials currently reported in the literature

Type	Material	Laser	Analyte	Contains MXene?	MXene load/ thickness	Linear range	LOD/ Sensitivity/ Enhancement	Recovery range/ reproducibility	Stability	Ref
SPR	MoS_2 + Au	N	Human IgG	No	–	5–20 μg mL^{-1}	19.7 ng mL^{-1}	Not specified	Tested for 5 cycles	242
	Muti-single fiber	633 nm	Glucose	No	–	0–10 mmol L^{-1}	0.12 mM L^{-1}, 2.819 nm mM^{-1}	Not specified	Not specified	243
	GO + Au NPs	400–1000 nm	DNA	No	–	1–1000 fmol	0.2 fM, 11773.93 nm per RIU	Not specified	Not specified	244
	Au + $Ti_3C_2T_x$ MXene	**633 nm**	**N**	**Yes**	**Not specified/ 4 layers**	**N**	**160°/ RIU, 16.8%**	**N**	**N**	166
	Ti_3C_2 MXene + AuNPs	633 nm	Carcinoembryonic antigen	No	–	20 fM–20 nM	0.07 fM	98.2–111.1%	7 days	245
SERS	GO + Au NPs	633 nm	Ampicillin	No	–	1–0.01 ng ml^{-1}	0.01 ng mL^{-1}	4.79% Std	Not specified	246
	Au@Ag + Au	633 nm 785 nm	Interleukin-6 (IL-6)	No	–	100 fg mL^{-1} to 1 ng mL^{-1}	12.4 fg mL^{-1}	92.4–105.3%	30 days	247
	CuO@Ag NPs	532 nm	Thiram	No	–	0.05–20 nmol L^{-1}	0.0067 nmol L^{-1}	93.9–112.3%, 10.33% Std	Not specified	235
	TiC MXene-decorated Au NPs	**532 nm**	**Chlorpromazine (CPZ)**	**Yes**	**Not specified**	**0.1 nmol L^{-1} to 0.1 mol L^{-1}**	**0.392 pmol L^{-1}**	**8.80% Std**	**15 days**	248
	Ti_2C MXene/Au–Ag NSs	**785 nm**	**Carbendazim (CBZ)**	**Yes**	**99.5% MXene**	**0.033– 10 μmol L^{-1}**	**0.01 μmol L^{-1}**	**2.77% Std**	**Not specified**	249
	Ag/r-GO/ZnO on nickel foam	N	H_2O_2	No	No	0.01–200 μmol L^{-1}	0.005 μmol L^{-1}	2.8% Std	25 days	250
	MoS_2/ZnO	N	Propyl gallate (PG)	No	No	0.125 μmol L^{-1} to 1.47 mmol L^{-1}	0.12 nmol L^{-1}	96–99.4%	Cycles for 30 times	251
	Carbon quantum dots (CDs)	365 nm EX/ 450 nm EM	Fe^{3+}	No	No	0.06–10 μmol L^{-1}	0.039 μmol L^{-1}	Not specified	Not specified	252
	g-C_3N_4	457 nm EX/ 588 nm EM	Zn^{2+}	No	No	10–2000 μM	1.8 μmol L^{-1}	Not specified	Not specified	253
Electrochemiluminescent and photoluminescent	TiO_2/$Ti_3C_2T_x$/Cu2O MXene	**N**	**Glucose**	**Yes**	**Not specified**	**100 nM– 10 mM**	**3.75** nM	**Not specified**	**Cycles for 400 s**	254
	$BiVO_4$/ $Ti_3C_2T_x$	**N**	**Hg^{2+}**	**Yes**	**Not specified**	**1 pM–2 nM**	**1 pM**	**90.7% and 109.3%**	**Cycles for 600 s**	255
	N-MQDs (Ti_3C_2)	**380 nm EX/ 570 nm EM**	**Cu^{2+}**	**Yes**	**100%**	**0–1000** μM	**3.0 nM**	**98.50–101.97%, 0.25–3.68% Std**	**30 days**	256
	Aptamer-polyhedraloligomericsilsesquioxane-perovskite QDs/ Ti_3C_2 MXenes composite	**480 nm EX/ 519 nm EM**	***Vibrio parahaemolyticus***	**Yes**	**Not specified**	**10^2–10^6 CFU mL^{-1}**	**100 CFU mL^{-1}**	**93% and 106%, 2.7–6.7% Std**	**1 week**	257

Text in bold refers to sensor materials containing MXene.

(LSPR). Density functional theory (DFT) studies support the IBT hypothesis, highlighting the peak's sensitivity to surface terminations while showing it to be largely independent of particle size[179] and solvent environment[180].

Evidence for LSPR contributions includes the detection of transverse plasmonic resonances via STEM-EELS[178] and voltage-induced blueshifts in electrochromic devices[181]. Ongoing and future studies are expected to clarify the underlying mechanisms and facilitate the continued development of MXene-based SERS substrates.

Electrochemiluminescent and photoluminescent sensors

In addition to plasmonic sensors, MXenes have also been investigated for their potential in luminescent sensing[182]. Luminescent sensors generate and separate charge carriers to produce an electrical signal upon light exposure. Due to high light absorption, efficient charge transport, and catalytic activity, MXenes have been employed as photoactive materials in these types of sensors to detect various analytes, such as heavy metals, organic pollutants, and biomolecules. In addition, MXenes have shown great promise as luminescent materials for biosensing, as their photoluminescence can be modulated through surface functionalization and interactions with target analytes. For instance, Ti_3C_2 MXene quantum dots detect metal ions and small molecules based on their photoluminescence quenching or enhancement effects[183].

However, MXenes also face challenges in photoluminescent sensing, such as weak photoluminescence efficiency, which limits sensitivity, and instability due to surface defects, oxidation, and degradation in aqueous environments. This issue can be addressed by doping MXene Quantum dots (MQDs) with metal or non-metal elements, like nitrogen, sulfur, or transition metals (*e.g.*, Mn and Cu), to alter their electronic properties and introduce new energy levels, thereby improving photoluminescent efficiency. For instance, a Cu ion sensor was developed using nitrogen-doped MQDs (N-MQDs), where PL quenching depended on Cu ion concentration[184]. Another sensor, made with nitrogen and phosphorus-doped MQDs, showed enhanced quenching and a low LOD for Cu ions. MQDs can also be detected in ions such as Fe and Cd[185].

$Ti_3C_2T_x$ is highly promising for fluorescence detection due to its excellent performance in fluorescence resonance energy transfer (FRET), serving as an effective energy acceptor and fluorescence quencher, making it ideal for MXene-based fluorescent aptasensors[186]. For instance, a $Ti_3C_2T_x$ MXene-based FRET aptasensor was demonstrated for thrombin detection using fluorescein amidite-labeled aptamers. The aptamers bind to $Ti_3C_2T_x$, enabling fluorescence quenching via FRET, demonstrating high sensitivity, specificity, and potential for clinical and bioactive molecule detection[187]. Other MXenes, such as FL-V_2CT_x and ML-V_2CT_x, have been explored for fluorescence sensors[188]. Few-layered MXenes offer improved adsorption and desorption capabilities due to their larger surface area, while multi-layered MXenes may face limitations, such as weaker fluorescence. However, the differences in performance between few- and multi-layered MXenes highlight the need for further investigation to optimize their use in fluorescence-based sensing applications. Although MXene-based aptasensors are promising, they remain in the early stages. Challenges such as short aptamer half-lives and a lack of diverse aptamers highlight the need for developing innovative strategies in future research[186].

Unlocking potential: exploring opportunities in unresolved challenges

The literature highlights efforts to address challenges in MXene-based sensors, yet unresolved barriers persist, which are discussed in this section (Fig. 6).

A standardized method of producing MXenes

Reviews on MXenes consistently emphasize that differences in synthesis methods and precursors result in variations in MXene properties[189–191]. MXenes etched with 50% HF or LiF/HCl exhibited different surface compositions, impacting their dispersibility[192]. Post-synthetic processes, including drying, can cause MXene to restack, altering its behavior. A solvent exchange technique could bypass drying for MXenes, enabling solution processing of MXene-based fiber composites[193]. These studies highlight how surface composition variations from different etching methods influence MXene performance in various solvent environments. Therefore, further research is needed to achieve uniform surface terminations and device architectures for specific sensing applications. Currently, surface modifications like covalent or noncovalent interactions with large molecules[194,195], surfactants[196], or polymers[35] are performed. These modifications are customized for specific techniques that require tailored surface properties and solvent interactions.

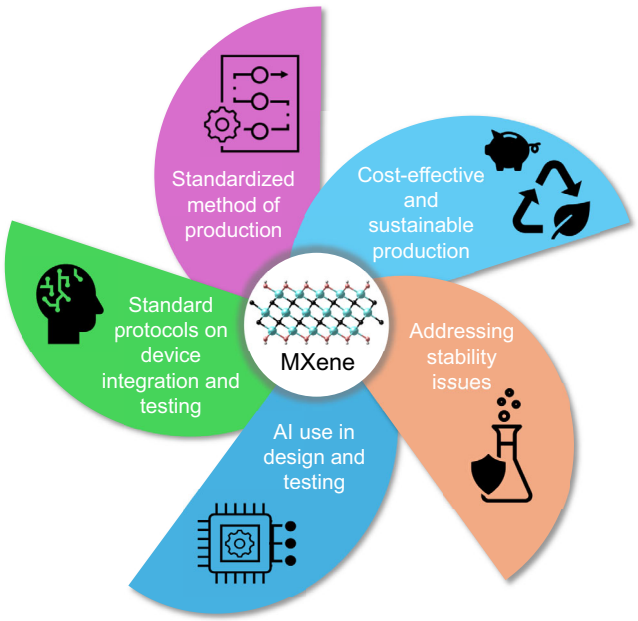

Fig. 6 | Future directions in MXene-based sensors. Schematic illustration summarizing the exciting research opportunities from remaining unresolved challenges in developing MXene-based sensors.

Cost-effective, scalable and sustainable production of MXenes

To make MXene-based sensors commercially viable, production must become more cost-effective and scalable without compromising performance. However, producing high-quality MXenes with consistent structural, chemical, and electrical properties at scale remains technically challenging and resource-intensive. Conventional methods, such as selective etching using hydrofluoric acid or in-situ HF generation, rely on hazardous chemicals, require precise reaction control, and generate significant chemical waste. These issues raise safety, environmental, and cost concerns.

To overcome these limitations, research is shifting toward more sustainable and economical strategies. One promising approach involves repurposing carbon-rich industrial byproducts or biomass to produce MAX phase precursors[197]. This approach not only reduces raw material costs but also aligns with circular economy goals by turning waste into valuable feedstock. At the same time, synthesis techniques are being optimized for large-scale production. Chemical vapor deposition (CVD), particularly with titanium tetrachloride ($TiCl_4$), a low-cost manufacturing precursor, offers a scalable, cleaner alternative to etching. CVD enables the direct synthesis of Cl-terminated MXenes, which show greater structural stability and oxidation resistance than conventional –OH, –O, or –F terminated MXenes from wet-etching methods[198].

Vapor-phase growth methods like CVD offer enhanced control over film thickness, crystallinity, and uniformity, which are parameters critical for device integration and reproducibility. CVD allows for precise engineering of surface terminations, opening new opportunities for tailoring MXene properties for specific sensing applications.

Life cycle assessments (LCAs) further support the need for synthesis optimization. Recent studies highlight that electricity consumption during production is a major contributor to environmental impact[199]. By simplifying synthesis, eliminating hazardous chemicals, and integrating process cost analysis, the overall sustainability and scalability of MXene production can be significantly improved.

As demand grows for flexible and wearable electronics, adopting scalable and environmentally sustainable methods like CVD becomes increasingly important. When combined with the use of industrial waste streams and streamlined synthesis protocols, these strategies represent a key step toward realizing the large-scale, reliable manufacturing of MXene-based sensors and devices.

Addressing MXene stability issues

MXenes are known to undergo surface degradation when exposed to water, resulting in the formation of oxide layers that compromise their electrical conductivity and overall performance[200]. Additionally, prolonged exposure to such conditions can lead to the loss of essential surface terminations, which are critical for their functionality. In practical device applications, MXene-based sensors are particularly vulnerable to harsh environmental conditions such as human sweat, body heat, and friction-induced mechanical stress[201]. Sweat, which contains water, salts, and various biomolecules, creates an electrolyte-rich environment that promotes the electrochemical oxidation of MXenes. Elevated temperatures from body heat further accelerate this degradation process. As oxidation progresses, surface oxides form, reducing the electrical conductivity and sensing capabilities of the material.

Mechanical stress from continuous movement, bending, and skin contact introduces shear forces that can lead to microcracks, delamination, or abrasion of protective coatings. These mechanical damages expose fresh MXene surfaces to ambient oxygen and moisture, which are highly reactive and prone to rapid oxidation. This results in a recurring degradation cycle. The combined effects of chemical exposure from sweat and mechanical wear are well-established contributors to the accelerated deterioration of MXene-based sensors[149], ultimately leading to reduced signal stability, increased noise, and diminished sensitivity and durability, thus limiting the long-term usability of wearable devices.

To enhance MXene stability, surface passivation and protective coatings such as polymers, self-assembled monolayers, or inorganic layers are commonly employed. While these approaches have shown short-term effectiveness, their long-term performance under real-world conditions remains uncertain due to a lack of extended experimental data[202–204]. Over time, passivation layers can degrade through mechanical abrasion, delamination, or the infiltration of oxygen and water molecules via microscopic defects or diffusion pathways. Once compromised, these layers expose the underlying MXene, restarting the degradation process.

Therefore, ensuring long-term reliability of MXene-based sensors requires further research into robust encapsulation strategies and implementation of realistic aging protocols. These efforts are essential to fully understand and address the time-dependent failure mechanisms of passivated MXene-based sensors in practical environments.

Large-scale integration and real-world testing

Integrating MXenes into devices while retaining their unique properties remains challenging. Key obstacles include achieving uniformity, ensuring compatibility with diverse substrates, and enabling scalable, efficient fabrication[205]. Despite notable progress, most studies remain confined to controlled laboratory environments that do not reflect real-world conditions.

To move MXene-based sensors toward commercial use, rigorous testing under diverse environmental conditions is essential. Scalability will depend on standardized protocols for material selection, device fabrication, and performance metrics like sensitivity, response time, and detection limits. Long-term reliability, mechanical durability, calibration consistency, and quality control are also critical to ensure manufacturability and real-world functionality.

Start-ups will play a key role in bridging the gap between research and commercialization. Their agility allows them to focus on targeted applications, refine production methods, and respond quickly to market demands. By fostering innovation across cross-sector collaboration, start-ups can accelerate product development and reduce the risks associated with early-stage technology.

This is particularly valuable in fast-moving fields of wearable electronics and smart systems, where user needs and supply chains are still evolving. With growing investment and interdisciplinary cooperation, start-ups are poised to drive the adoption of MXene-based sensors in next-generation intelligent and flexible technologies.

Potential use of artificial intelligence in design and testing

The rapid advancement of artificial intelligence (AI) offers great potential for enhancing MXene-based sensors, driving improvements in design, optimization, and overall performance. AI can serve as a tool for refining key aspects of fabrication, such as material density, surface uniformity, and electrode placement, ensuring consistency and preserving signal integrity. Through AI-driven design and modeling, complex interactions between sensor components can be analyzed, leading to more efficient, reliable, and cost-effective sensor development. Furthermore, AI's ability to process large datasets allows for the identification of hidden patterns, relationships, and anomalies during fabrication and testing. This optimization can enable continuous, real-time data analysis, supporting personalized and highly responsive monitoring. Integrating AI with MXene sensor research could expand their capabilities, offering dynamic, accessible, and impactful solutions for environmental monitoring, healthcare, and many other applications.

However, it is important to emphasize that the success of AI models heavily depends on the quality and reliability of the underlying sensor data. If sensor systems are not stable or consistent over time, they can produce noisy, incomplete, or inaccurate datasets. Such compromised data will negatively impact the training process of AI algorithms, leading to models that perform poorly when applied to real-world conditions. This limitation can reduce the predictive accuracy, generalizability, and robustness of AI-driven solutions, ultimately hindering their practical utility. Therefore, ensuring the development of reliable, durable, and high-quality MXene sensors is a critical prerequisite for effective AI integration. Without this foundation, the benefits of AI in improving sensor performance, scalability, and application-specific customization will be significantly diminished, underscoring the need for continued research focused on sensor stability and reproducibility.

Summary and conclusion

Substantial progress has been made in advancing MXene-based sensors, setting the stage for their potential commercialization. Nonetheless, industrial-scale production and application still face significant obstacles. Although $Ti_3C_2T_x$ MXenes are highly responsive active materials for physical sensors (e.g., strain and pressure), they are primarily limited by mechanical stability. Fortunately, their compatibility with polymers and their ability to form films, fibers, or aerogels allows for versatile sensor designs. Integrating MXenes into 3D structures enhances mechanical properties, increases surface area, and improves sensitivity to dynamic loading and deformation. Improved coating techniques for enhanced substrate compatibility help mitigate issues like delamination and damage during repeated physical processes, further enhancing durability and functionality. On the other hand, MXenes face challenges in force-sensitive sensing applications like acoustic, temperature, and photoresponsive detection due to excessive conductivity. Hybrid nanomaterial structures are addressing these issues by enhancing performance and adding functionalities beyond the intrinsic capabilities of MXenes. Meanwhile, chemical and electrochemical sensors based on MXenes often struggle with limited mass transport to active sites due to their tendency to layer and restack. Additionally, MXenes' susceptibility to oxidation compromises performance in chemical environments. Active materials and interlayer spacers are integrated into MXenes to improve mass transport, prevent oxidation, and

reduce issues with conductivity and capacitive behavior, thus enhancing analyte signal detection. Optical and spectroscopic sensors relying on MXenes' electromagnetic properties require highly uniform chemical structures and surfaces. Strategies such as surface modifications and composite materials can be employed to address this. However, the interfacial interactions between MXenes and functional materials, as well as the fundamental issues in MXene-based optical sensors, require further investigation and remain a complex area of ongoing research. Moreover, the commercialization of MXene-based sensors is hindered by costly, hazardous synthesis, stability issues like oxidation, and scalability challenges. The lack of real-world testing in existing studies also poses a challenge. Overall, tackling these issues is expected to accelerate the development of next-generation MXene-based sensors.

Received: 18 February 2025; Accepted: 28 July 2025;
Published online: 29 September 2025

References

1. Anasori, B., Lukatskaya, M. R. & Gogotsi, Y. 2D metal carbides and nitrides (MXenes) for energy storage. *Nat. Rev. Mater.* **2**, 16098 (2017).
2. Han, M. et al. Beyond $Ti_3C_2T_x$: MXenes for electromagnetic interference shielding. *ACS Nano* **14**, 5008–5016 (2020).
3. Usman, K. A. S. et al. $Ti_3C_2T_x$ MXene: from dispersions to multifunctional architectures for diverse applications. *Mater. Horiz.* **8**, 2886–2912 (2021).
4. Anasori, B. & Gogotsi, Y. The global expansion of MXenes. *Graphene 2D Mater.* **8**, 39–41 (2023).
5. Thakur, A. & Anasori, B. Accelerating 2D materials discovery. *Science* **383**, 1182–1183 (2024).
6. Shayesteh Zeraati, A. et al. Improved synthesis of $Ti_3C_2T_x$ MXenes resulting in exceptional electrical conductivity, high synthesis yield, and enhanced capacitance. *Nanoscale* **13**, 3572–3580 (2021).
7. Mathis, T. S. et al. Modified MAX phase synthesis for environmentally stable and highly conductive $Ti_3C_2T_x$ MXene. *ACS Nano* **15**, 6420–6429 (2021).
8. Zhang, J. et al. in *MXenes* (ed. Gogotsi, Y.) 519–538 (Jenny Stanford Publishing, 2023).
9. Yang, C. et al. Flexible nitrogen-doped 2D titanium carbides (MXene) films constructed by an ex situ solvothermal method with extraordinary volumetric capacitance. *Adv. Energy Mater.* **8**, 1802087 (2018).
10. Zhang, P. et al. Integrated textile supercapacitors enhanced with energy-absorbing spacer fabrics and $Ti_3C_2T_x$ MXene. *Adv. Funct. Mater.* **34**, 2403601 (2024).
11. Yang, F. et al. A nitrogenous pre-intercalation strategy for the synthesis of nitrogen-doped $Ti_3C_2T_x$ MXene with enhanced electrochemical capacitance. *J. Mater. Chem. A* **9**, 6393–6401 (2021).
12. Krishnamoorthy, R., Muthumalai, K., Nagaraja, T., Rajendrakumar, R. T. & Das, S. R. Chemically exfoliated titanium carbide MXene for highly sensitive electrochemical sensors for detection of 4-nitrophenols in drinking water. *ACS Omega* **7**, 42644–42654 (2022).
13. Le, V. T. et al. Flexible and high-sensitivity sensor based on Ti_3C_2–MoS_2 MXene composite for the detection of toxic gases. *Chemosphere* **291**, 133025 (2022).
14. Li, M. et al. Flexible accelerated-wound-healing antibacterial MXene-based epidermic sensor for intelligent wearable human–machine interaction. *Adv. Funct. Mater.* **32**, 2208141 (2022).
15. Yang, L. et al. Wearable pressure sensors based on mxene/tissue papers for wireless human health monitoring. *ACS Appl. Mater. Interfaces* **13**, 60531–60543 (2021).
16. Li, L. et al. Hydrophobic and stable MXene–polymer pressure sensors for wearable electronics. *ACS Appl. Mater. Interfaces* **12**, 15362–15369 (2020).
17. Wu, M. et al. Ti_3C_2 MXene-based sensors with high selectivity for NH_3 detection at room temperature. *ACS Sensors* **4**, 2763–2770 (2019).
18. Chen, W. Y. et al. Surface functionalization of $Ti_3C_2T_x$ MXene with highly reliable superhydrophobic protection for volatile organic compounds sensing. *ACS Nano* **14**, 11490–11501 (2020).
19. Ma, X. et al. Hierarchical porous MXene/amino carbon nanotubes-based molecular imprinting sensor for highly sensitive and selective sensing of fisetin. *Sens. Actuators B: Chem.* **309**, 127815 (2020).
20. Gopal, T. S. et al. MXene-based composite electrodes for efficient electrochemical sensing of glucose by non-enzymatic method. *Mater. Today Chem.* **24**, 100891 (2022).
21. Ho, D. H., Choi, Y. Y., Jo, S. B., Myoung, J.-M. & Cho, J. H. Sensing with MXenes: progress and prospects. *Adv. Mater.* **33**, 2005846 (2021).
22. Zhu, M. et al. Hollow MXene sphere/reduced graphene aerogel composites for piezoresistive sensor with ultra-high sensitivity. *Adv. Electron. Mater.* **6**, 1901064 (2020).
23. Wang, K. et al. Bioinspired interlocked structure-induced high deformability for two-dimensional titanium carbide (MXene)/natural microcapsule-based flexible pressure sensors. *ACS Nano* **13**, 9139–9147 (2019).
24. Qiu, Z. et al. Molecularly imprinted polymer functionalized Bi_2S_3/$Ti_3C_2T_x$ MXene nanocomposites for photoelectrochemical/electrochemical dual-mode sensing of chlorogenic acid. *Chemosensors* **10**, 252 (2022).
25. Shin, H., Lee, H., Seo, Y., Jeong, W. & Han, T. H. Grafting behavior of amine ligands for surface modification of MXene. *Langmuir* **39**, 2358–2367 (2023).
26. Zhao, L., Wang, K., Wei, W., Wang, L. & Han, W. High-performance flexible sensing devices based on polyaniline/MXene nanocomposites. *InfoMat* **1**, 407–416 (2019).
27. Zhang, Z. et al. Durable and highly sensitive flexible sensors for wearable electronic devices with PDMS-MXene/TPU composite films. *Ceram. Int.* **48**, 4977–4985 (2022).
28. Zhang, L. et al. Highly sensitive capacitive flexible pressure sensor based on a high-permittivity MXene nanocomposite and 3D network electrode for wearable electronics. *ACS Sensors* **6**, 2630–2641 (2021).
29. Xu, X. et al. Wearable CNT/$Ti_3C_2T_x$ MXene/PDMS composite strain sensor with enhanced stability for real-time human healthcare monitoring. *Nano Res.* **14**, 2875–2883 (2021).
30. Jia, B. et al. Highly-sensitive, broad-range, and highly-dynamic MXene pressure sensors with multi-level nano-microstructures for healthcare and soft robots applications. *Chem. Eng. J.* **485**, 149750 (2024).
31. Wang, Y. et al. Hierarchically buckled $Ti_3C_2T_x$ MXene/carbon nanotubes strain sensor with improved linearity, sensitivity, and strain range for soft robotics and epidermal monitoring. *Sens. Actuators B: Chem.* **368**, 132228 (2022).
32. Hajian, S., Maddipatla, D., Narakathu, B. B. & Atashbar, M. Z. MXene-based flexible sensors: a review. *Front. Sens*. **3**, https://doi.org/10.3389/fsens.2022.1006749 (2022).
33. Riazi, H., Taghizadeh, G. & Soroush, M. MXene-based nanocomposite sensors. *ACS Omega* **6**, 11103–11112 (2021).
34. Guo, Z. et al. High electrical conductivity 2D MXene serves as additive of Perovskite for efficient solar cells. *Small* **14**, 1802738 (2018).
35. Lee, J. T. et al. Covalent surface modification of $Ti_3C_2T_x$ MXene with chemically active polymeric ligands producing highly conductive and ordered microstructure films. *ACS Nano* **15**, 19600–19612 (2021).
36. Pendyala, P., Lee, J., Kim, S. J. & Yoon, E.-S. Layer-dependent frictional properties of $Ti_3C_2T_x$ MXene nanosheets. *Appl. Surf. Sci.* **603**, 154402 (2022).

37. Li, X. et al. Multi-stimuli-responsive $Ti_3C_2T_x$ MXene-based actuators actualizing intelligent interpretation of traditional shadow play. *Carbon* **218**, 118652 (2024).
38. Liu, P. et al. Humidity sensor based on tapered no-core fiber coated with $Ti_3C_2T_x$ MXene. *Ceram. Int.* **50**, 23586–23592 (2024).
39. Bi, M., Miao, Y., Li, W. & Yao, J. Niobium carbide MXene-optics fiber-sensor for high sensitivity humidity detection. *Appl. Phys. Lett*. **120**, https://doi.org/10.1063/5.0064005 (2022).
40. Shi, Z. et al. MXene fibers-based molecularly imprinted disposable electrochemical sensor for sensitive and selective detection of hydrocortisone. *Talanta* **266**, 125100 (2024).
41. Yu, X.-f et al. Monolayer $T_{i2}CO_2$: a promising candidate for NH_3 sensor or capturer with high sensitivity and selectivity. *ACS Appl. Mater. Interfaces* **7**, 13707–13713 (2015).
42. Xiao, B., Li, Y.-c, Yu, X.-f & Cheng, J.-b MXenes: reusable materials for NH_3 sensor or capturer by controlling the charge injection. *Sens. Actuators B: Chem.* **235**, 103–109 (2016).
43. Liu, F. et al. Preparation and methane adsorption of two-dimensional carbide Ti_2C. *Adsorption* **22**, 915–922 (2016).
44. Liu, F. et al. Preparation of Ti_3C_2 and Ti_2C MXenes by fluoride salts etching and methane adsorptive properties. *Appl. Surf. Sci.* **416**, 781–789 (2017).
45. Chen, J. et al. CO_2 and temperature dual responsive "Smart" MXene phases. *Chem. Commun.* **51**, 314–317 (2015).
46. Rizwan, K., Rahdar, A., Bilal, M. & Iqbal, H. M. N. MXene-based electrochemical and biosensing platforms to detect toxic elements and pesticides pollutants from environmental matrices. *Chemosphere* **291**, 132820 (2022).
47. Dhillon, A., Singh, N., Nair, M. & Kumar, D. Analytical methods to determine and sense heavy metal pollutants using MXene and MXene-based composites: mechanistic prophecy into sensing properties. *Chemosphere* **303**, 135166 (2022).
48. Chen, Y. et al. A portable multi-signal readout sensing platform based on plasmonic MXene induced signal amplification for point of care biomarker detection. *Sens. Actuators B: Chem.* **352**, 131059 (2022).
49. Wang, Y. et al. $Ti_3C_2T_x$ MXene-based flexible piezoresistive physical sensors. *ACS Nano* **16**, 1734–1758 (2022).
50. Yang, Y. et al. MXenes for wearable physical sensors toward smart healthcare. *ACS Nano* **18**, 24705–24740 (2024).
51. Iravani, S. Role of MXenes in advancing soft robotics. *Soft Matter* **19**, 6196–6212 (2023).
52. Liu, L. et al. Recent advances of flexible MXene physical sensor to wearable electronics. *Mater. Today Commun.* **35**, 106014 (2023).
53. Jia, L. et al. Tuning MXene electrical conductivity towards multifunctionality. *Chem. Eng. J.* **475**, 146361 (2023).
54. Li, C. et al. Highly efficient, remarkable sensor activity and energy storage properties of MXenes and borophene nanomaterials. *Prog. Solid State Chem.* **70**, 100392 (2023).
55. Gautschi, G. in *Piezoelectric Sensorics: Force Strain Pressure Acceleration and Acoustic Emission Sensors Materials and Amplifiers* (ed. Gautschi, G.) 127–140 (Springer, Berlin, Heidelberg, 2002).
56. Duan, L., D'Hooge, D. R. & Cardon, L. Recent progress on flexible and stretchable piezoresistive strain sensors: from design to application. *Prog. Mater. Sci.* **114**, 100617 (2020).
57. Seyedin, S. et al. MXene composite and coaxial fibers with high stretchability and conductivity for wearable strain sensing textiles. *Adv. Funct. Mater.* **30**, 1910504 (2020).
58. Yang, Y. et al. $Ti_3C_2T_x$ MXene-graphene composite films for wearable strain sensors featured with high sensitivity and large range of linear response. *Nano Energy* **66**, 104134 (2019).
59. Yang, K. et al. A highly flexible and multifunctional strain sensor based on a network-structured MXene/polyurethane mat with ultra-high sensitivity and a broad sensing range. *Nanoscale* **11**, 9949–9957 (2019). **This paper presents the first demonstration of a flexible, stretchable network-MXene/Polyurethane mat as a strain sensor, achieving exceptional sensitivity (gauge factor up to 228), wide sensing range (150%), and durability (3200 cycles)**.
60. Uzun, S. et al. Knittable and washable multifunctional MXene-coated cellulose yarns. *Adv. Funct. Mater.* **29**, 1905015 (2019). **This work presents one of the best-performing prototypes of washable, MXene-coated cellulose yarns for textile electronics, enabling a fully knitted capacitive pressure sensor with high sensitivity, wide sensing range, and excellent cycling stability**.
61. Yang, Y., Shi, L., Cao, Z., Wang, R. & Sun, J. Strain sensors with a high sensitivity and a wide sensing range based on a $Ti_3C_2T_x$ (MXene) nanoparticle–nanosheet hybrid network. *Adv. Funct. Mater.* **29**, 1807882 (2019).
62. Jia, Z. et al. Constructing conductive titanium carbide nanosheet (MXene) network on polyurethane/polyacrylonitrile fibre framework for flexible strain sensor. *J Colloid Interface Sci.* **584**, 1–10 (2021).
63. Guo, H. et al. Thickness-induced gradient micro-wrinkle PDMS/MXene/rGO wearable strain sensor with high sensitivity and stretchability for human motion detection. *Chem. Eng. J.* **495**, 153684 (2024).
64. Leong, W. X. R., Al-Dhahebi, A. M., Ahmad, M. R. & Saheed, M. S. M. $Ti_3C_2T_x$ MXene-polymeric strain sensor with huge gauge factor for body movement detection. *Micromachines* **13**, 1302 (2022).
65. Lei, D. et al. Roles of MXene in pressure sensing: preparation, composite structure design, and mechanism. *Adv. Mater.* **34**, 2110608 (2022).
66. Ma, Y. et al. 3D Synergistical MXene/reduced graphene oxide aerogel for a piezoresistive sensor. *ACS Nano* **12**, 3209–3216 (2018).
67. Yuan, H. et al. Progress and challenges in flexible capacitive pressure sensors: microstructure designs and applications. *Chem. Eng. J.* **485**, 149926 (2024).
68. Sharma, S., Chhetry, A., Sharifuzzaman, M., Yoon, H. & Park, J. Y. Wearable capacitive pressure sensor based on MXene composite nanofibrous scaffolds for reliable human physiological signal Acquisition. *ACS Appl. Mater. Interfaces* **12**, 22212–22224 (2020). **This study is among the first to sandwich MXene /poly(vinylidene fluoride-trifluoroethylene) (PVDF-TrFE) composites into piezoelectric polymers for capacitive sensors, achieving high sensitivity, ultralow detection limits, and durability for physiological monitoring and human–machine interfaces**.
69. Wang, S. et al. Boosting piezoelectric response of PVDF-TrFE via MXene for self-powered linear pressure sensor. *Compos. Sci. Technol.* **202**, 108600 (2021).
70. Kim, K. N. et al. All-printed wearable triboelectric nanogenerator with ultra-charged electron accumulation polymers based on MXene nanoflakes. *Adv. Electron. Mater.* **8**, 2200819 (2022). **This study reports the first all-printed, sustainable wearable triboelectric nanogenerator (TENG) prototype using MXene-based electron accumulation polymers, achieving a sixfold performance boost, superior charge retention, and reliable operation for powering portable electronics and real-time pH monitoring**.
71. Lei, D. et al. An ion channel-induced self-powered flexible pressure sensor based on potentiometric transduction mechanism. *Adv. Funct. Mater.* **32**, 2108856 (2022). **This work pioneers an all-solid-state, self-powered pressure sensor using MXene-integrated nanofibers, achieving wide detection range (0.7 Pa–1300 kPa), high stability, and real-time physiological signal monitoring without external power, offering a new design paradigm for next-generation electronic and healthcare devices**.
72. Zhuo, H. et al. A carbon aerogel with super mechanical and sensing performances for wearable piezoresistive sensors. *J. Mater. Chem. A* **7**, 8092–8100 (2019).
73. Liu, R. et al. MXene-coated air-permeable pressure-sensing fabric for smart wear. *ACS Appl. Mater. Interfaces* **12**, 46446–46454 (2020).

This study presents a high-performance, washable MXene-coated cotton fabric pressure sensor with strong interfacial bonding, achieving a high gauge factor (7.67 kPa^{-1}), fast response (<35 ms), excellent stability (>2000 cycles), and durability, enabling its use in multitouch wearable human–machine interfaces.

74. Yang, N. et al. Flexible pressure sensor decorated with MXene and reduced graphene oxide composites for motion detection, information transmission, and pressure sensing performance. *ACS Appl. Mater. Interfaces* **14**, 45978–45987 (2022).
75. Lin, Z. et al. Insights into materials, physics, and applications in flexible and wearable acoustic sensing technology. *Adv. Mater.* **36**, 2306880 (2024).
76. Gou, G.-Y. et al. Two-stage amplification of an ultrasensitive MXene-based intelligent artificial eardrum. *Sci. Adv.* **8**, eabn2156 (2022). **This study is among the earliest to use MXene for artificial implants, demonstrating an ultrasensitive artificial eardrum with 62 kPa^{-1} sensitivity and 0.1 Pa detection limit, enabling high-accuracy real-time voice recognition for wearable acoustic healthcare applications**.
77. Lai, Q.-T. et al. Emerging MXene-based flexible tactile sensors for health monitoring and haptic perception. *Small* **19**, 2300283 (2023).
78. Chen, J. et al. An intelligent MXene/MoS_2 acoustic sensor with high accuracy for mechano-acoustic recognition. *Nano Res.* **16**, 3180–3187 (2023).
79. Chai, Z., Fang, M. & Min, X. Composite phase-change materials for photo-thermal conversion and energy storage: a review. *Nano Energy* **124**, 109437 (2024).
80. Tran, M. H. et al. Synthesis of a smart hybrid MXene with switchable conductivity for temperature sensing. *ACS Appl. Nano Mater.* **3**, 4069–4076 (2020).
81. Anasori, B. et al. Control of electronic properties of 2D carbides (MXenes) by manipulating their transition metal layers. *Nanoscale Horiz.* **1**, 227–234 (2016).
82. Cao, Z. et al. Highly flexible and sensitive temperature sensors based on $Ti_3C_2T_x$ (MXene) for electronic skin. *J. Mater. Chem. A* **7**, 25314–25323 (2019).
83. Zhao, L. et al. Tissue-like sodium alginate-coated 2D MXene-based flexible temperature sensors for full-range temperature monitoring. *Adv. Mater. Technol.* **7**, 2101740 (2022).
84. Fu, J. et al. Large stroke radially oriented MXene composite fiber tensile artificial muscles. *Sci. Adv.* **11**, eadt1560 (2025).
85. Chertopalov, S. & Mochalin, V. N. Environment-sensitive photoresponse of spontaneously partially oxidized Ti_3C_2 MXene thin films. *ACS Nano* **12**, 6109–6116 (2018). **This study demonstrates that partially oxidized MXene – TiO_2 thin films exhibit strong UV photoresponse and long-lasting charge retention (~24 h), making them promising materials for photoresistors with memory effects and environmental sensitivity**.
86. Xiao, X., Ma, H. & Zhang, X. Flexible photodriven actuator based on gradient–paraffin-wax-filled $Ti_3C_2T_x$ MXene film for bionic robots. *ACS Nano* **15**, 12826–12835 (2021).
87. Luo, X.-J. et al. Multifunctional $Ti_3C_2T_x$ MXene/low-density polyethylene soft robots with programmable configuration for amphibious motions. *ACS Appl. Mater. Interfaces* **13**, 45833–45842 (2021).
88. Murugan, N., Jerome, R., Preethika, M., Sundaramurthy, A. & Sundramoorthy, A. K. 2D-titanium carbide (MXene) based selective electrochemical sensor for simultaneous detection of ascorbic acid, dopamine and uric acid. *J. Mater. Sci.* **72**, 122–131 (2021).
89. Liu, M. et al. A label-free molecularly imprinted electrochemical sensor based on MXene nanosheets modified by gold nanoparticles for sensitive and selective detection of homocysteine. *J. Electrochem. Soc.* **169**, 087503 (2022).
90. Rajeev, R. & Varghese, A. High-performance β-cyclodextrin-$Ti_3C_2T_x$ MXene-based electrochemical sensor for the detection of neurological disorder biomarker. *J. Electrochem. Soc.* **171**, 027504 (2024).
91. Duan, H., Tang, S.-Y., Goda, K. & Li, M. Enhancing the sensitivity and stability of electrochemical aptamer-based sensors by AuNPs@MXene nanocomposite for continuous monitoring of biomarkers. *Biosens. Bioelectron.* **246**, 115918 (2024).
92. Liu, Y. et al. Fast and in-situ electrodeposition of MXene/AuNPs composite for multiplexed and sensitive detection of infectious biomarkers using an electrochemical biosensor. *Microchem J.* **207**, 112064 (2024).
93. Dmytriv, T. R. & Lushchak, V. I. Potential biosafety of Mxenes: stability, biodegradability, toxicity and biocompatibility. *Chem. Rec.* **24**, e202300338 (2024).
94. Lim, G. P. et al. Cytotoxicity of MXene-based nanomaterials for biomedical applications: a mini review. *Environ. Res.* **201**, 111592 (2021).
95. Kim, S. J. et al. Metallic $Ti_3C_2T_x$ MXene gas sensors with ultrahigh signal-to-noise ratio. *ACS Nano* **12**, 986–993 (2018). **This study highlights the superior performance of MXene gas sensors, achieving ultra-low detection limits (50–100 ppb) for volatile organic compounds at room temperature and a signal-to-noise ratio two orders of magnitude higher than other 2D materials**.
96. Sun, S. et al. $W_{18}O_{49}/Ti_3C_2T_x$ Mxene nanocomposites for highly sensitive acetone gas sensor with low detection limit. *Sens. Actuators B: Chem.* **304**, 127274 (2020).
97. Zhu, L.-Y. et al. Highly sensitive and stable MEMS acetone sensors based on well-designed α-Fe_2O_3/C mesoporous nanorods. *J Colloid Interface Sci.* **622**, 156–168 (2022).
98. Xiao, X. et al. Rational synthesis and gas sensing performance of ordered mesoporous semiconducting WO_3/NiO composites. *ACS Appl. Mater. Interfaces* **11**, 26268–26276 (2019).
99. Choi, J. H. et al. Graphene-based gas sensors with high sensitivity and minimal sensor-to-sensor variation. *ACS Appl. Nano Mater.* **3**, 2257–2265 (2020).
100. Zubiarrain-Laserna, A. et al. Detection of free chlorine in water using graphene-like carbon based chemiresistive sensors. *RSC Adv.* **12**, 2485–2496 (2022).
101. Alali, K. T. et al. HFIP-functionalized 3D carbon nanostructure as chemiresistive nerve agents sensors under visible light. *Sens. Actuators B: Chem.* **358**, 131475 (2022).
102. Lee, E., VahidMohammadi, A., Yoon, Y. S., Beidaghi, M. & Kim, D.-J. Two-dimensional vanadium carbide MXene for gas sensors with ultrahigh sensitivity toward nonpolar gases. *ACS Sensors* **4**, 1603–1611 (2019).
103. Najafi, P. & Ghaemi, A. Chemiresistor gas sensors: design, challenges, and strategies: a comprehensive review. *Chem. Eng. J.* **498**, 154999 (2024).
104. Mirzaei, A., Kim, J.-Y., Kim, H. W. & Kim, S. S. Resistive gas sensors based on 2D TMDs and MXenes. *Acc. Chem. Res.* **57**, 2395–2413 (2024).
105. Park, H. et al. Fast-response electrochemical biosensor based on a truncated aptamer and MXene heterolayer for West Nile virus detection in human serum. *Bioelectrochemistry* **154**, 108540 (2023).
106. Lee, E. et al. Room temperature gas sensing of two-dimensional titanium carbide (MXene). *ACS Appl. Mater. Interfaces* **9**, 37184–37190 (2017). **This study presents the first MXene-based gas sensors, demonstrating room-temperature detection of ethanol, methanol, acetone, and ammonia using MXene nanosheets on flexible substrates, with p-type sensing behavior, a low theoretical detection limit for acetone (9.27 ppm), and performance surpassing other 2D material-based sensors**.

107. Sardana, S., Debnath, A. K., Aswal, D. K. & Mahajan, A. WS_2 nanosheets decorated multi-layered MXene based chemiresistive sensor for efficient detection and discrimination of NH_3 and NO_2. *Sens. Actuators B: Chem.* **394**, 134352 (2023).
108. Li, L. et al. First-principles study of Ti-deficient Ti_3C_2 MXene nanosheets as NH_3 gas sensors. *ACS Appl. Nano Mater.* **5**, 2470–2475 (2022).
109. Zhao, W.-N., Yun, N., Dai, Z.-H. & Li, Y.-F. A high-performance trace level acetone sensor using an indispensable $V_4C_3T_x$ MXene. *RSC Adv.* **10**, 1261–1270 (2020).
110. Wang, L. et al. Ultra-high performance humidity sensor enabled by a self-assembled CuO/$Ti_3C_2T_x$ MXene. *RSC Adv.* **13**, 6264–6273 (2023).
111. An, H. et al. Water sorption in MXene/polyelectrolyte multilayers for ultrafast humidity sensing. *ACS Appl. Nano Mater.* **2**, 948–955 (2019).
112. Li, X. et al. Onion-inspired MXene/chitosan-quercetin multilayers: enhanced response to H_2O molecules for wearable human physiological monitoring. *Sens. Actuators B: Chem.* **329**, 129209 (2021).
113. Li, T. et al. A high-performance humidity sensor based on alkalized MXenes and poly(dopamine) for touchless sensing and respiration monitoring. *J. Mater. Chem. C* **10**, 2281–2289 (2022).
114. Yuan, W., Yang, K., Peng, H., Li, F. & Yin, F. A flexible VOCs sensor based on a 3D Mxene framework with a high sensing performance. *J. Mater. Chem. A* **6**, 18116–18124 (2018).
115. Chen, W. Y., Jiang, X., Lai, S.-N., Peroulis, D. & Stanciu, L. Nanohybrids of a MXene and transition metal dichalcogenide for selective detection of volatile organic compounds. *Nat. Commun.* **11**, 1302 (2020). **This study demonstrates the use of hybrid 2D materials, combining MXene with WSe_2, to create a flexible, low-noise VOC sensor with ultrafast response and over 12-fold improved ethanol sensitivity, while also enhancing MXene stability and guiding future designs of high-performance, field-deployable sensors**.
116. Zou, S. et al. Enhanced gas sensing properties at low working temperature of iron molybdate/MXene composite. *J Alloys Compd.* **817**, 152785 (2020).
117. Xia, T., Liu, G., Wang, J., Hou, S. & Hou, S. MXene-based enzymatic sensor for highly sensitive and selective detection of cholesterol. *Biosens. Bioelectron.* **183**, 113243 (2021).
118. Muckley, E. S. et al. Multimodality of structural, electrical, and gravimetric responses of intercalated MXenes to water. *ACS Nano* **11**, 11118–11126 (2017).
119. Pei, Y. et al. $Ti_3C_2T_x$ MXene for sensing applications: recent progress, design principles, and future perspectives. *ACS Nano* **15**, 3996–4017 (2021).
120. Li, N. et al. High-performance humidity sensor based on urchin-like composite of Ti_3C_2 MXene-derived TiO_2 nanowires. *ACS Appl. Mater. Interfaces* **11**, 38116–38125 (2019). **This study highlights the enhanced sensing performance of a MXene/TiO_2 composite humidity sensor, featuring** in situ **grown TiO_2 nanowires that boost surface area and achieve record-high sensitivity (~280 pF/%RH) in low humidity, enabling noncontact detection of liquids and human presence**.
121. Jiang, Y., Wu, L., Chen, Q., Li, N. & Tian, J. High-performance capacitive humidity sensor based on flower-like SnS_2/Ti_3C_2 MXene for respiration monitoring and non-contact sensing. *Sens. Actuators B: Chem.* **426**, 137012 (2025).
122. Li, N. et al. A fully inkjet-printed transparent humidity sensor based on a Ti_3C_2/Ag hybrid for touchless sensing of finger motion. *Nanoscale* **11**, 21522–21531 (2019).
123. Liu, H. A., Li, N., Jiang, Y., Wang, Q. & Peng, Z. Plasma treated MXene/Ag-based humidity sensor with ultrahigh sensitivity for gesture tracking. *IOP Conf. Ser. Mater. Sci.* **563**, 022046 (2019).
124. Yang, M.-Y et al. Printing assembly of flexible devices with oxidation stable MXene for high performance humidity sensing applications. *Sens. Actuators B: Chem.* **364**, 131867 (2022).
125. Zhang, H.-W et al. Interlayer cross-linked MXene enables ultra-stable printed paper-based flexible sensor for real-time humidity monitoring. *Chem. Eng. J.* **495**, 153343 (2024).
126. Shao, Y. et al. Two-dimensional MXene nanosheets (types $Ti_3C_2T_x$ and Ti_2CT_x) as new ion-to-electron transducers in solid-contact calcium ion-selective electrodes. *Microchim. Acta* **186**, 750 (2019).
127. Simões, F. R. & Xavier, M. G. in *Nanoscience and its Applications* (eds Da Róz, A.L., Ferreira, M., Leite, F. d. L. & Oliveira, O. N.) 155-178 (William Andrew Publishing, 2017).
128. Zahran, M., Khalifa, Z., Zahran, M. A. H. & Abdel Azzem, M. Recent advances in silver nanoparticle-based electrochemical sensors for determining organic pollutants in water: a review. *Mater. Adv.* **2**, 7350–7365 (2021).
129. Cardoso, A. G. et al. Electrochemical sensing of analytes in saliva: challenges, progress, and perspectives. *Trends Anal. Chem.* **160**, 116965 (2023).
130. Lee, J., Kim, M. C., Soltis, I., Lee, S. H. & Yeo, W.-H. Advances in electrochemical sensors for detecting analytes in biofluids. *Adv. Sens. Res.* **2**, 2200088 (2023).
131. Sulthana, S. F. et al. Electrochemical sensors for heavy metal ion detection in aqueous medium: a systematic review. *ACS Omega* **9**, 25493–25512 (2024).
132. Chuang, C.-H. & Kung, C.-W. Metal-organic frameworks toward electrochemical sensors: challenges and opportunities. *Electroanalysis* **32**, 1885–1895 (2020).
133. Kajal, N., Singh, V., Gupta, R. & Gautam, S. Metal organic frameworks for electrochemical sensor applications: a review. *Environ. Res.* **204**, 112320 (2022).
134. Zhao, L. Horseradish peroxidase labelled-sandwich electrochemical sensor based on ionic liquid-gold nanoparticles for *Lactobacillus brevis*. *Micromachines* **12**, 75 (2021).
135. Li, X. et al. Preparation and application of electrochemical horseradish peroxidase sensor based on a black phosphorene and single-walled carbon nanotubes nanocomposite. *Molecules* **27**, 8064 (2022).
136. Mani, V., Devadas, B. & Chen, S.-M. Direct electrochemistry of glucose oxidase at electrochemically reduced graphene oxide-multiwalled carbon nanotubes hybrid material modified electrode for glucose biosensor. *Biosens. Bioelectron.* **41**, 309–315 (2013).
137. Kang, X. et al. Glucose Oxidase–graphene–chitosan modified electrode for direct electrochemistry and glucose sensing. *Biosens. Bioelectron.* **25**, 901–905 (2009).
138. Lu, Y. et al. Aptamer-based electrochemical sensors with aptamer-complementary DNA oligonucleotides as probe. *Anal. Chem.* **80**, 1883–1890 (2008).
139. Yang, Y., Yang, X., Yang, Y. & Yuan, Q. Aptamer-functionalized carbon nanomaterials electrochemical sensors for detecting cancer relevant biomolecules. *Carbon* **129**, 380–395 (2018).
140. Pernites, R. B., Venkata, S. K., Tiu, B. D. B., Yago, A. C. C. & Advincula, R. C. Nanostructured, molecularly imprinted, and template-patterned polythiophenes for chiral sensing and differentiation. *Small* **8**, 1669–1674 (2012).
141. Raziq, A. et al. Development of a portable MIP-based electrochemical sensor for detection of SARS-CoV-2 antigen. *Biosens. Bioelectron.* **178**, 113029 (2021).
142. Wang, L., Pagett, M. & Zhang, W. Molecularly imprinted polymer (MIP) based electrochemical sensors and their recent advances in health applications. *Sens. Actuators Rep.* **5**, 100153 (2023).
143. Kalambate, P. K. et al. Progress, challenges, and opportunities of two-dimensional layered materials based electrochemical sensors and biosensors. *Mater. Today Chem.* **26**, 101235 (2022).

144. Kalambate, P. K. et al. Recent advances in MXene-based electrochemical sensors and biosensors. *Trends Anal. Chem.* **120**, 115643 (2019).
145. Huang, Y., Afolabi, M. A., Gan, L., Liu, S. & Chen, Y. MXene-coated ion-selective electrode sensors for highly stable and selective lithium dynamics monitoring. *Environ. Sci. Technol.* **58**, 1359–1368 (2024).
146. Yu, Z. et al. Application of superhydrophobic Ti_3C_2 Mxene-based screen-printed ion-selective electrode for determination of Ca^{2+} concentration. *Surf. Interfaces* **42**, 103500 (2023).
147. Zhang, J. et al. 3D porous structure assembled from MXene via breath figure method for electrochemical detection of dopamine. *Chem. Eng. J.* **452**, 139414 (2023).
148. Gu, H. et al. Three-dimensional porous $T_{i3}C_2T_x$ MXene–graphene hybrid films for glucose biosensing. *ACS Appl. Nano Mater* **2**, 6537–6545 (2019).
149. Marquez, K. P. et al. Understanding the chemical degradation of $Ti_3C_2T_x$ MXene dispersions: a chronological analysis. *Small Sci.* **4**, 2400150 (2024).
150. Okubo, M., Sugahara, A., Kajiyama, S. & Yamada, A. MXene as a charge storage host. *Acc. Chem. Res.* **51**, 591–599 (2018).
151. Tang, J. et al. Tuning the electrochemical performance of titanium carbide MXene by controllable in situ anodic oxidation. *Angew. Chem. Int. Ed.* **58**, 17849–17855 (2019).
152. Noriega, N. et al. Pristine $Ti_3C_2T_x$ MXene enables flexible and transparent electrochemical sensors. *ACS Appl. Mater. Interfaces* **16**, 6569–6578 (2024).
153. Cao, J., Zhang, H., Nian, Q. & Xu, Q. Electrospun chitosan/polyethylene oxide nanofibers mat loaded with copper (II) as a new sensor for colorimetric detection of tetracycline. *Int. J. Biol. Macromol.* **212**, 527–535 (2022).
154. Fazli, Y., Shariatinia, Z., Kohsari, I., Azadmehr, A. & Pourmortazavi, S. M. A novel chitosan-polyethylene oxide nanofibrous mat designed for controlled co-release of hydrocortisone and imipenem/cilastatin drugs. *Int. J. Pharm.* **513**, 636–647 (2016).
155. Kalasin, S. & Sangnuang, P. Multiplex wearable electrochemical sensors fabricated from sodiated polymers and mxene nanosheet to measure sodium and creatinine levels in sweat. *ACS Appl. Nano Mater.* **6**, 18209–18221 (2023). **This pioneering work presents the first integration of sodiated MXene with redox active conductive polymers for dual sodium ion and creatinine biosensing in a stretchable epidermal wearable, achieving ultra-low signal drift, high stability over 3000 cycles, and real time sweat analysis**.
156. Raab, C., Rieger, J., Ghosh, A., Spellberg, J. L. & King, S. B. Surface plasmons in two-dimensional MXenes. *J. Phys. Chem. Lett.* **15**, 11643–11656 (2024).
157. Song, Q. et al. Graphene and MXene nanomaterials: toward high-performance electromagnetic wave absorption in gigahertz band range. *Adv. Funct. Mater.* **30**, 2000475 (2020).
158. Chaudhuri, K. et al. Highly broadband absorber using plasmonic titanium carbide (MXene). *ACS Photonics* **5**, 1115–1122 (2018).
159. Tan, K. H., Samylingam, L., Aslfattahi, N., Saidur, R. & Kadirgama, K. Optical and conductivity studies of polyvinyl alcohol–MXene (PVA–MXene) nanocomposite thin films for electronic applications. *Opt. Laser Technol.* **136**, 106772 (2021).
160. Zhou, J. et al. Two-dimensional nanomaterial-based plasmonic sensing applications: Advances and challenges. *Coord. Chem. Rev.* **410**, 213218 (2020).
161. Phuong, N. T. T., Tho, L. H., Nguyen, T. T., Nam, N. N. & Trinh, K. T. L. Application of M, 114714xenes and their composites in plasmon-enhanced optical sensors: review paper. *Sens. Actuators A: Phys.* **363**, 114714 (2023).
162. Shukla, N., Chetri, P., Boruah, R., Gogoi, A. & Ahmed, G. A. in *Recent Advances in Plasmonic Probes: Theory and Practice* (eds Biswas, R. & Mazumder, N.) 191–222 (Springer International Publishing, 2022).
163. Xue, Y. et al. Polyphosphoramide-intercalated MXene for simultaneously enhancing thermal stability, flame retardancy and mechanical properties of polylactide. *Chem. Eng. J.* **397**, 125336 (2020).
164. Chithravel, A. et al. 2D material assisted prism based surface plasmon resonance sensors: a comprehensive survey. *Opt. Lasers Eng.* **182**, 108452 (2024).
165. Shrivastav, A. M. et al. Engineering the penetration depth of nearly guided wave surface plasmon resonance towards application in bacterial cells monitoring. *Sens. Actuators B: Chem.* **345**, 130338 (2021).
166. Wu, L. et al. Few-layer $Ti_3C_2T_x$ MXene: a promising surface plasmon resonance biosensing material to enhance the sensitivity. *Sens. Actuators B: Chem.* **277**, 210–215 (2018). **This study presents the first use of MXene in surface plasmon resonance (SPR) biosensors, demonstrating significant sensitivity enhancement across various metal substrates and wavelengths, highlighting MXene's potential as a novel 2D material for high-performance SPR-based biosensing applications**.
167. Srivastava, S., Singh, S., Mishra, A. C., Lohia, P. & Dwivedi, D. K. Numerical study of titanium dioxide and MXene nanomaterial-based surface plasmon resonance biosensor for virus SARS-CoV-2 detection. *Plasmonics* **18**, 1477–1488 (2023). **This study demonstrates the use of MXene in a plasmonic biosensor for SARS-CoV-2 detection, integrating Ag, TiO_2, and MXene nanolayers in a Kretschmann SPR configuration to achieve ultrahigh angular sensitivity (346°/RIU)**.
168. Hasanah, L. et al. Investigating the effect of surface termination and thickness of MXene on the detection response of the SPR sensor using FDTD simulation. *Results Opt.* **12**, 100438 (2023).
169. Li, M. et al. Halogenated Ti_3C_2 MXenes with electrochemically active terminals for high-performance zinc ion batteries. *ACS Nano* **15**, 1077–1085 (2021).
170. Schultz, T. et al. Surface termination dependent work function and electronic properties of $Ti_3C_2T_x$ MXene. *Chem. Mater.* **31**, 6590–6597 (2019).
171. Muhammed, M. M. & Mokkath, J. H. Surface termination dependent optical characteristics of MXene nanoflakes. *Mater. Today Chem.* **29**, 101447 (2023).
172. Sarycheva, A. et al. Two-dimensional titanium carbide (MXene) as surface-enhanced raman scattering substrate. *J. Phys. Chem. C* **121**, 19983–19988 (2017). **This pioneering work demonstrates the first use of MXene as a substrate for surface-enhanced Raman spectroscopy (SERS), achieving enhancement factors up to ~ 10^6 for detecting organic dyes in both solid and solution phases, and highlighting MXene's potential for biomedical and environmental sensing applications**.
173. Yang, Y.-Y. et al. Terminal groups-dependent near-field enhancement effect of $Ti_3C_2T_x$ nanosheets. *Nanoscale Res. Lett.* **16**, 1–7 (2021).
174. Limbu, T. B. et al. Unravelling the thickness dependence and mechanism of surface-enhanced raman scattering on $Ti_3C_2T_x$ MXene nanosheets. *J. Phys. Chem. C* **124**, 17772–17782 (2020).
175. Ye, Y. et al. Remarkable surface-enhanced Raman scattering of highly crystalline monolayer Ti_3C_2 nanosheets. *Sci. China Mater. Sci.* **63**, 794–805 (2020).
176. Satheeshkumar, E. et al. One-step solution processing of Ag, Au and Pd@ MXene hybrids for SERS. *Sci. Rep.* **6**, 32049 (2016).
177. Xie, H. et al. Electrostatic self-assembly of $Ti_3C_2T_x$ MXene and gold Nanorods as an efficient surface-enhanced Raman scattering platform for reliable and high-sensitivity determination of organic pollutants. *ACS Sensors* **4**, 2303–2310 (2019).
178. El-Demellawi, J. K., Lopatin, S., Yin, J., Mohammed, O. F. & Alshareef, H. N. Tunable multipolar surface plasmons in 2D $Ti_3C_2T_x$ MXene flakes. *ACS Nano* **12**, 8485–8493 (2018).

179. Maleski, K., Ren, C. E., Zhao, M.-Q., Anasori, B. & Gogotsi, Y. Size-dependent physical and electrochemical properties of two-dimensional MXene flakes. *ACS Appl. Mater. Interfaces* **10**, 24491–24498 (2018).
180. Maleski, K., Mochalin, V. N. & Gogotsi, Y. Dispersions of two-dimensional titanium carbide MXene in organic solvents. *Chem. Mater.* **29**, 1632–1640 (2017).
181. Salles, P. et al. Electrochromic effect in titanium carbide MXene thin films produced by dip-coating. *Adv. Funct. Mater* **29**, 1809223 (2019).
182. Liu, X. et al. Rapid determination of SARS-CoV-2 nucleocapsid proteins based on 2D/2D MXene/P–BiOCl/Ru(bpy)$_3^{2+}$ heterojunction composites to enhance electrochemiluminescence performance. *Anal. Chim. Acta* **1234**, 340522 (2022).
183. Wang, Y. et al. Titanium carbide MXenes mediated in situ reduction allows label-free and visualized nanoplasmonic sensing of silver ions. *Anal. Chem.* **92**, 4623–4629 (2020).
184. Feng, Y., Zhou, F., Deng, Q. & Peng, C. Solvothermal synthesis of in situ nitrogen-doped Ti_3C_2 MXene fluorescent quantum dots for selective Cu^{2+} detection. *Ceram. Int.* **46**, 8320–8327 (2020). **This study highlights the use of nitrogen-doped Ti_3C_2 MXene quantum dots (QDs) for selective ion detection, demonstrating strong fluorescence-quenching response to Cu^{2+} and showcasing the potential of combining MXene and QDs for high-sensitivity optical sensing applications**.
185. Guan, Q. et al. Highly fluorescent Ti_3C_2 MXene quantum dots for macrophage labeling and Cu^{2+} ion sensing. *Nanoscale* **11**, 14123–14133 (2019).
186. Zahra, Qu. A. et al. MXene-based aptasensors: advances, challenges, and prospects. *Prog. Mater. Sci.* **129**, 100967 (2022).
187. Cui, H., Fu, X., Yang, L., Xing, S. & Wang, X.-F. 2D titanium carbide nanosheets based fluorescent aptasensor for sensitive detection of thrombin. *Talanta* **228**, 122219 (2021).
188. Zhu, T. et al. Sensitive determination of prostate-specific antigen with graphene quantum dot-based fluorescence aptasensor using few-layer V_2CT_x MXene as quencher. *Spectrochim. Acta A* **293**, 122474 (2023).
189. Lim, K. R. G. et al. Fundamentals of MXene synthesis. *Nat. Synth.* **1**, 601–614 (2022).
190. Lakmal, A., Thombre, P. B. & Shuck, C. E. Solid-solution MXenes: synthesis, properties, and applications. *Acc. Chem. Res.* **57**, 3007–3019 (2024).
191. Bi, W., Gao, G., Li, C., Wu, G. & Cao, G. Synthesis, properties, and applications of MXenes and their composites for electrical energy storage. *Prog. Mater. Sci.* **142**, 101227 (2024).
192. Benchakar, M. et al. One MAX phase, different MXenes: a guideline to understand the crucial role of etching conditions on $Ti_3C_2T_x$ surface chemistry. *Appl. Surf. Sci.* **530**, 147209 (2020).
193. Seyedin, S. et al. Facile solution processing of stable MXene dispersions towards conductive composite fibers. *Glob. Chall.* **3**, 1900037 (2019).
194. Jing, H. et al. Modulation of the electronic properties of MXene ($Ti_3C_2T_x$) via surface-covalent functionalization with diazonium. *ACS Nano* **15**, 1388–1396 (2021).
195. Huang, H. et al. Recent development and prospects of surface modification and biomedical applications of MXenes. *Nanoscale* **12**, 1325–1338 (2020).
196. Wang, X. et al. Surface hydrophobic modification of MXene to promote the electrochemical conversion of N_2 to NH_3. *J. Energy Chem.* **87**, 439–449 (2023).
197. Shuck, C. E. et al. Effect of Ti_3AlC2 MAX phase on structure and properties of resultant $Ti_3C_2T_x$ MXene. *ACS Appl. Nano Mater.* **2**, 3368–3376 (2019).
198. Wang, D. et al. Direct synthesis and chemical vapor deposition of 2D carbide and nitride MXenes. *Science* **379**, 1242–1247 (2023).
199. Dadashi Firouzjaei, M. et al. Life-cycle assessment of $Ti_3C_2T_x$ MXene synthesis. *Adv. Mater.* **35**, 2300422 (2023).
200. Lipatov, A. et al. Effect of synthesis on quality, electronic properties and environmental stability of individual monolayer Ti_3C_2 MXene flakes. *Adv. Electron. Mater.* **2**, 1600255 (2016).
201. Yang, J. et al. Wearable temperature sensor with moisture resistance based on MXene-embedded fiber. *AIP Adv*. **14**, https://doi.org/10.1063/5.0178843 (2024).
202. Yoon, J. et al. Biocompatible and oxidation-resistant $Ti_3C_2T_x$ MXene with halogen-free surface terminations. *Small Methods* **7**, 2201579 (2023).
203. Zhao, H., Ding, J., Zhou, M. & Yu, H. Air-stable titanium carbide MXene nanosheets for corrosion protection. *ACS Appl. Nano Mater.* **4**, 3075–3086 (2021).
204. Zhang, M., Héraly, F., Yi, M. & Yuan, J. Multitasking tartaric-acid-enabled, highly conductive, and stable MXene/conducting polymer composite for ultrafast supercapacitor. *Cell Rep. Phys. Sci*. **2**, https://doi.org/10.1016/j.xcrp.2021.100449 (2021).
205. Katiyar, A. K. et al. 2D Materials in flexible electronics: recent advances and future prospectives. *Chem. Rev*. **124**, 318–419 (2024).
206. He, J. et al. A universal high accuracy wearable pulse monitoring system via high sensitivity and large linearity graphene pressure sensor. *Nano Energy* **59**, 422–433 (2019).
207. Wang, Z. et al. High sensitivity, wearable, piezoresistive pressure sensors based on irregular microhump structures and its applications in body motion sensing. *Small* **12**, 3827–3836 (2016).
208. Gao, J. et al. Ultrastretchable multilayered fiber with a hollow-monolith structure for high-performance strain sensor. *ACS Appl. Mater. Interfaces* **10**, 34592–34603 (2018).
209. Zhai, K. et al. High-performance strain sensors based on organohydrogel microsphere film for wearable human–computer interfacing. *Adv. Sci.* **10**, 2205632 (2023).
210. Wang, H. et al. High-performance foam-shaped strain sensor based on carbon nanotubes and $Ti_3C_2T_x$ MXene for the monitoring of human activities. *ACS Nano* **15**, 9690–9700 (2021).
211. Mohseni Taromsari, S., Shi, H. H., Saadatnia, Z., Park, C. B. & Naguib, H. E. Design and development of ultra-sensitive, dynamically stable, multi-modal GnP@MXene nanohybrid electrospun strain sensors. *Chem. Eng. J.* **442**, 136138 (2022).
212. Bai, N. et al. Graded intrafillable architecture-based iontronic pressure sensor with ultra-broad-range high sensitivity. *Nat. Commun.* **11**, 209 (2020).
213. Lv, L., Zhang, P., Xu, T. & Qu, L. Ultrasensitive pressure sensor based on an ultralight sparkling graphene block. *ACS Appl. Mater. Interfaces* **9**, 22885–22892 (2017).
214. Yang, M. et al. High-performance flexible pressure sensor with a self-healing function for tactile feedback. *Adv. Sci.* **9**, 2200507 (2022).
215. Li, X. et al. Ultracomfortable hierarchical nanonetwork for highly sensitive pressure sensor. *ACS Nano* **14**, 9605–9612 (2020).
216. Gao, L. et al. Highly sensitive pseudocapacitive iontronic pressure sensor with broad sensing range. *Nanomicro Lett.* **13**, 140 (2021).
217. Lang, C., Fang, J., Shao, H., Ding, X. & Lin, T. High-sensitivity acoustic sensors from nanofibre webs. *Nat. Commun.* **7**, 11108 (2016).
218. Xiang, Z. et al. High-performance microcone-array flexible piezoelectric acoustic sensor based on multicomponent lead-free perovskite rods. *Matter* **6**, 554–569 (2023).
219. Yang, H. et al. High-sensitive and ultra-wide spectrum multifunctional triboelectric acoustic sensor for broad scenario applications. *Nano Energy* **104**, 107932 (2022).
220. Lee, S. et al. A high-fidelity skin-attachable acoustic sensor for realizing auditory electronic skin. *Adv. Mater.* **34**, 2109545 (2022).
221. Xie, Y. et al. 3D MXene-based flexible network for high-performance pressure sensor with a wide temperature range. *Adv. Sci.* **10**, 2205303 (2023).

222. Niu, Y. et al. Design and performance evaluation of an all-ceramic high-temperature test sensor. *J Alloys Compd.* **938**, 168561 (2023).
223. Lin, M. et al. A high-performance, sensitive, wearable multifunctional sensor based on rubber/CNT for human motion and skin temperature detection. *Adv. Mater.* **34**, 2107309 (2022).
224. Liu, Z. et al. A temperature sensor based on flexible substrate with ultra-high sensitivity for low temperature measurement. *Sens. Actuators A: Phys.* **315**, 112341 (2020).
225. Yu, Y., Peng, S., Blanloeuil, P., Wu, S. & Wang, C. H. Wearable temperature sensors with enhanced sensitivity by engineering microcrack morphology in PEDOT:PSS–PDMS sensors. *ACS Appl. Mater. Interfaces* **12**, 36578–36588 (2020).
226. Ran, W. et al. An integrated flexible all-nanowire infrared sensing system with record photosensitivity. *Adv. Mater.* **32**, 1908419 (2020).
227. Kim, M. S. et al. High-sensitivity organic photodetector based on surface-concentrated nonfused ring electron acceptor. *Adv. Opt. Mater.* **11**, 2202525 (2023).
228. Han, C. et al. High-performance phototransistor based on graphene/organic heterostructure for in-chip visual processing and pulse monitoring. *Adv. Funct. Mater.* **32**, 2209680 (2022).
229. Fang, H. et al. A chemiresistive ppt level NO_2 gas sensor based on CeO_2 nanoparticles modified CuO nanosheets operated at 100 °C. *Sens. Actuators B: Chem.* **393**, 134277 (2023).
230. Suematsu, K. et al. Pulse-driven semiconductor gas sensors toward ppt level toluene detection. *Anal. Chem.* **90**, 11219–11223 (2018).
231. Verma, G. et al. Flexible hybrid nanostructured chemiresistive sensing platform for low-temperature trace hydrogen detection. *Sens. Actuators B: Chem.* **422**, 136621 (2025).
232. Liu, J. et al. Label-free chemiresistive sensors based on self-assembled $Ti_3C_2T_x$ MXene films for monitoring of microcystin-LR in water samples. *Environ. Sci. Technol.* **57**, 15432–15442 (2023).
233. Song, Z. et al. High-sensitivity paper-based capacitive humidity sensors for respiratory monitoring. *IEEE Sens. J.* **23**, 2291–2302 (2023).
234. Zhang, X., He, D., Yang, Q. & Atashbar, M. Z. Rapid, highly sensitive, and highly repeatable printed porous paper humidity sensor. *Chem. Eng. J.* **433**, 133751 (2022).
235. Duan, Z., Li, J., Yuan, Z., Jiang, Y. & Tai, H. Capacitive humidity sensor based on zirconium phosphate nanoplates film with wide sensing range and high response. *Sens. Actuators B: Chem.* **394**, 134445 (2023).
236. Soliman, M. A., Mahmoud, A. M., Elzanfaly, E. S. & Abdel Fattah, L. E. Electrochemical sensor based on bio-inspired molecularly imprinted polymer for sofosbuvir detection. *RSC Adv.* **13**, 25129–25139 (2023).
237. Chen, J., Tan, L., Qu, K., Cui, Z. & Wang, J. Novel electrochemical sensor modified with molecularly imprinted polymers for determination of enrofloxacin in marine environment. *Microchim. Acta* **189**, 95 (2022).
238. Madhu, S. et al. SnO_2 nanoflakes deposited carbon yarn-based electrochemical immunosensor towards cortisol measurement. *J. Nanostructure Chem.* **13**, 115–127 (2023).
239. Wang, F. et al. Lamellar Ti_3C_2 MXene composite decorated with platinum-doped MoS_2 nanosheets as electrochemical sensing functional platform for highly sensitive analysis of organophosphorus pesticides. *Food Chem.* **459**, 140379 (2024).
240. Liu, H. et al. Molecularly imprinted electrochemical sensors based on $Ti_3C_2T_x$-MXene and graphene composite modifications for ultrasensitive cortisol detection. *Anal. Chem.* **95**, 16079–16088 (2023).
241. Wang, H. et al. A label-free electrochemical biosensor for highly sensitive detection of gliotoxin based on DNA nanostructure/MXene nanocomplexes. *Biosens. Bioelectron.* **142**, 111531 (2019).
242. Song, H., Wang, Q. & Zhao, W.-M. A novel SPR sensor sensitivity-enhancing method for immunoassay by inserting MoS_2 nanosheets between metal film and fiber. *Opt. Lasers Eng.* **132**, 106135 (2020).
243. Xu, Y. et al. High linearity temperature-compensated SPR fiber sensor for the detection of glucose solution concentrations. *Opt. Laser Technol.* **169**, 110133 (2024).
244. Chen, S., Liu, Y., Yu, Q. & Peng, W. Self-referencing SPR biosensing with an ultralow limit-of-detection using long-wavelength excitation. *Sens. Actuators B: Chem.* **327**, 128935 (2021).
245. Wu, Q. et al. A 2D transition metal carbide MXene-based SPR biosensor for ultrasensitive carcinoembryonic antigen detection. *Biosens. Bioelectron.* **144**, 111697 (2019).
246. Wang, Y., Chen, H. & Jiang, L. A highly reproducible SERS sensor based on an Au nanoparticles/graphene oxide hybrid nanocomposite for label-free quantitative detection of antibiotics. *Analyst* **146**, 5740–5746 (2021).
247. Li, A. et al. Digital SERS immunoassay of Interleukin-6 based on Au@Ag-Au nanotags. *Biosens. Bioelectron.* **270**, 116973 (2025).
248. Barveen, N. R., Wang, T.-J. & Chang, Y.-H. A photochemical approach to anchor Au NPs on MXene as a prominent SERS substrate for ultrasensitive detection of chlorpromazine. *Microchim. Acta* **189**, 16 (2021).
249. Zhu, X. et al. A novel graphene-like titanium carbide MXene/Au–Ag nanoshuttles bifunctional nanosensor for electrochemical and SERS intelligent analysis of ultra-trace carbendazim coupled with machine learning. *Ceram. Int.* **47**, 173–184 (2021).
250. Tao, B., Gao, B., Miao, F. & Zang, Y. Synthesis of Ag/r-GO/ZnO nanocomposite on nickel foam for achieving efficient photoelectrochemical sensing of hydrogen peroxide. *Vacuum* **211**, 111953 (2023).
251. Han, F. et al. MoS_2/ZnO-heterostructures-based label-free, visible-light-excited photoelectrochemical sensor for sensitive and selective determination of synthetic antioxidant propyl gallate. *Anal. Chem.* **91**, 10657–10662 (2019).
252. Xu, Z. et al. Facile synthesis of N-doped carbon dots for direct/indirect detection of heavy metal ions and cell imaging. *Environ. Sci. Pollut. Res.* **28**, 19878–19889 (2021).
253. Ahmed, A., John, P., Nawaz, M. H., Hayat, A. & Nasir, M. Zinc-doped mesoporous graphitic carbon nitride for colorimetric detection of hydrogen peroxide. *ACS Appl. Mater. Interfaces* **2**, 5156–5168 (2019).
254. Chen, G. et al. Efficient Z-Scheme heterostructure based on TiO_2/$Ti_3C_2T_x$/Cu_2O to boost photoelectrochemical response for ultrasensitive biosensing. *Sens. Actuators B: Chem.* **312**, 127951 (2020).
255. Jiang, Q. et al. Efficient $BiVO_4$ photoanode decorated with $Ti_3C_2T_X$ MXene for enhanced photoelectrochemical sensing of Hg(II) ion. *Anal. Chim. Acta* **1119**, 11–17 (2020).
256. Zhou, X. et al. Nitrogen-doped Ti_3C_2 MXene quantum dots as an effective FRET ratio fluorometric probe for sensitive detection of Cu^{2+} and D-PA. *Spectrochim. Acta A* **293**, 122484 (2023).
257. Hong, J. et al. A turn-on–type fluorescence resonance energy transfer aptasensor for vibrio detection using aptamer-modified polyhedral oligomeric silsesquioxane-perovskite quantum dots/Ti_3C_2 MXenes composite probes. *Microchim. Acta* **188**, 45 (2021).

Author contributions

Y. Yao mainly conducted the literature search and prepared the first draft of the paper. X. Li mainly conducted the literature search and prepared the first draft of the paper. K.M.D. Sisican contributed to writing, revising the contents of the manuscript. M. Judicpa contributed to writing, revising the contents of the manuscript. R.M.C. Ramos contributed to writing, revising the contents of the manuscript. J. Zhang contributed to writing, revising the contents of the manuscript. S. Qin contributed to writing, revising the contents of the manuscript. J. Yao supervised, reviewed, edited the paper, and acquired the funding. J.M. Razal supervised, reviewed, edited the paper, and acquired the funding. K.A.S. Usman proposed the idea and conceived the outline of the manuscript, conducted the literature search and prepared the first draft of the paper.

Competing interests
The authors declare no competing interests.

Inclusion and Ethics statement
This work is a review article and does not involve original research with human participants, local data collection, or material transfer. Nevertheless, we affirm our adherence to the principles of equity, inclusion, and ethical authorship as outlined by the Global Code of Conduct for Research in Resource-Poor Settings and the Nature Portfolio guidelines on authorship and collaboration.

Additional information
Supplementary information The online version contains supplementary material available at https://doi.org/10.1038/s43246-025-00907-y.

Correspondence and requests for materials should be addressed to Juming Yao, Joselito M. Razal or Ken Aldren S. Usman.

Peer review information *Communications Materials* thanks Sagnik Basuray, Jinbo Pang and Arnab Hazra for their contribution to the peer review of this work. Primary Handling Editors: Mengqiang Zhao and John Plummer. A peer review file is available.

Reprints and permissions information is available at http://www.nature.com/reprints

Publisher's note Springer Nature remains neutral with regard to jurisdictional claims in published maps and institutional affiliations.

Open Access This article is licensed under a Creative Commons Attribution-NonCommercial-NoDerivatives 4.0 International License, which permits any non-commercial use, sharing, distribution and reproduction in any medium or format, as long as you give appropriate credit to the original author(s) and the source, provide a link to the Creative Commons licence, and indicate if you modified the licensed material. You do not have permission under this licence to share adapted material derived from this article or parts of it. The images or other third party material in this article are included in the article's Creative Commons licence, unless indicated otherwise in a credit line to the material. If material is not included in the article's Creative Commons licence and your intended use is not permitted by statutory regulation or exceeds the permitted use, you will need to obtain permission directly from the copyright holder. To view a copy of this licence, visit http://creativecommons.org/licenses/by-nc-nd/4.0/.

© The Author(s) 2025